

**Optical Beam Diagnosis at ELSA
Based on a Streak Camera System
with Picosecond Temporal Resolution**

Michael T. Switka

Masterarbeit in Physik
angefertigt im Physikalischen Institut

vorgelegt der
Mathematisch-Naturwissenschaftlichen Fakultät
der
Rheinischen Friedrich-Wilhelms-Universität
Bonn

NOV 2013

I hereby declare that this thesis was formulated by myself and that no sources or tools other than those cited were used.

Bonn,
Date

.....
Signature

1. Gutachter: PD Dr. Wolfgang Hillert
2. Gutachter: Prof. Dr. Jochen Dingfelder

Contents

1	Introduction	1
2	Charged Particle Beam Dynamics In Electron Storage Rings & Imaging Techniques	5
2.1	Particle Motion	5
2.1.1	Transverse Motion	6
2.1.2	Effects of Synchrotron Radiation & Longitudinal Motion	9
2.1.3	Beam Equilibria & Beam Dimensions	11
2.2	Nature of Synchrotron Radiation	13
2.2.1	Radial Distribution	13
2.2.2	Spectral Distribution	14
2.3	Imaging Techniques	16
2.3.1	Geometric Optics	16
2.3.2	Transverse & Longitudinal Resolution	16
2.3.3	Operation Principle of a Streak Camera	17
3	The M7 Diagnostic Beamline	21
3.1	The Source Point	21
3.2	The Photon Beamline	22
3.3	Diagnostics Section	24
3.4	The Streak Camera System	28
4	Measurements	31
4.1	Slow Sweep	31
4.2	Synchroscan	33
4.2.1	Bunch Length & Longitudinal Phase	34
4.2.2	Grow-Damp-Measurements	36
4.2.3	ELSA at High Beam Currents	38
5	Summary and Outlook	39
A	Appendix	41
A.1	Technical Drawing of the M7 dipole section	41
A.2	Streak Camera Photo Cathode Response	41
	Bibliography	45

List of Figures	47
List of Tables	49
Acknowledgements	51

Introduction

The 3.5 GeV electron pulse stretcher accelerator ELSA provides spin polarized and unpolarized electrons for hadron physics experiments. Electron accelerators have been operated by the Physics Institute of Bonn University since 1958.[HIL06] The pulse stretcher ring ELSA was added to the existing periphery in 1987. The stretcher ring injector system follows a typical scheme: A LINAC¹ accelerates a 50 keV electron beam from the polarizing or thermal source up to 26 MeV. It is then injected into the booster synchrotron [ALT67] for further acceleration and extracted into ELSA at an energy of 1.2 GeV. ELSA accumulates and stores the electron bunches. Three different modes of operation are available:

- In *pulse stretcher mode* the electrons remain at injection energy. The accumulated bunches are evenly distributed around the storage ring and slowly extracted for experimental usage. A duty factor² towards 100 % is achievable.
- The *post accelerator mode* allows modification of the beam energy between 0.5–3.5 GeV. A fast energy ramp of up to 7 GeV/s is applied after injection, followed by a slow extraction process. This is the standard operation mode of ELSA providing a duty factor of 60–80 %.
- In *storage mode* the beam is accumulated, ramped to the corresponding energy and stored for up to several hours. Since the appearance of *third generation* synchrotron light sources³ with higher beam brilliance this mode is nowadays primarily used for machine studies requiring stable beam intensities.

ELSA is currently the primary instrumentation device for the nuclear physics program of Bonn University and the German Research Foundation within the Collaborative Research Center Transregio 16 (CRC TRR 16). [THOb] It contributes to the scientific exploration of the subnuclear structure of matter and intrinsically to the field of accelerator physics. Two experimental stations are supplied by an extracted electron beam of approximately 1 nA beam current. Both stations are used for tagged photon experiments, namely the Crystal-Barrel [THO05] and BGO-OD [SCH10] experiment.

Responding to the demands of electron beam irradiation, e.g. for detector testing, two beamlines are currently in commissioning. The high energy irradiation beamline will be supplied by electrons

¹ Linear accelerator

² Time of beam delivered to the experiment divided by total time of cycle.

³ Facilities built for synchrotron radiation production only.

extracted from ELSA. A low energy irradiation station is installed at the injector beamline of LINAC 1 (20 MeV).

The ELSA facility is illustrated in Fig. 1.1. Table 2.1 gives an overview of important machine parameters.

The instrumentation development project D.2 of the CRC TRR 16 supports studies for a rise of beam polarization, beam current and quality. [THOa] The subsequent development constantly enhances the machine's subsystems, including its diagnostics. Amongst other features, ELSA is operated with state of the art controls, bunch-by-bunch feedback and precise beam measurement systems. Current developments include the extension of the RF⁴ system for the storage and extraction of higher beam currents at high energies, an upgrade of the injector LINAC 1 in order to provide single bunch injection and the extension of the beam diagnosis capabilities.

In order to satisfy the requirements for beam quality and stability, non-destructive beam diagnosis is essential. However, monitoring systems based on capacitive or inductive beam interaction usually meet their resolution limits when sampling beyond nanosecond intervals is required. The length of the electron distribution in synchrotrons is usually in the range of picoseconds, thus making it impossible to be resolved by capacitive or inductive monitoring systems.

An alternative monitoring approach is the utilization of synchrotron radiation. This radiation is intensely generated by electron deflection within the bending magnets of a synchrotron. The emitted light yields precise 3-dimensional information about the electron distribution in the machine. The limit of its resolution is given by the optical image processing system. Today, streak camera systems offer temporal resolutions down to one picosecond, thus increasing the diagnostic capabilities by three orders of magnitudes when comparing to capacitive systems. The imaging of single bunches and their dynamics in time windows ranging from nanoseconds to several milliseconds becomes available. Instability studies will be used to implement optimized settings of the accelerator's operation parameters.

This document describes the set-up and operation performance of the newly installed streak camera system at ELSA. In order to understand the measurement results, the properties of the source point, the optical transfer beamline and the streak camera are explained in the following chapters.

⁴ Radio frequency, e.g. 500 MHz

Electron Stretcher Accelerator (ELSA)

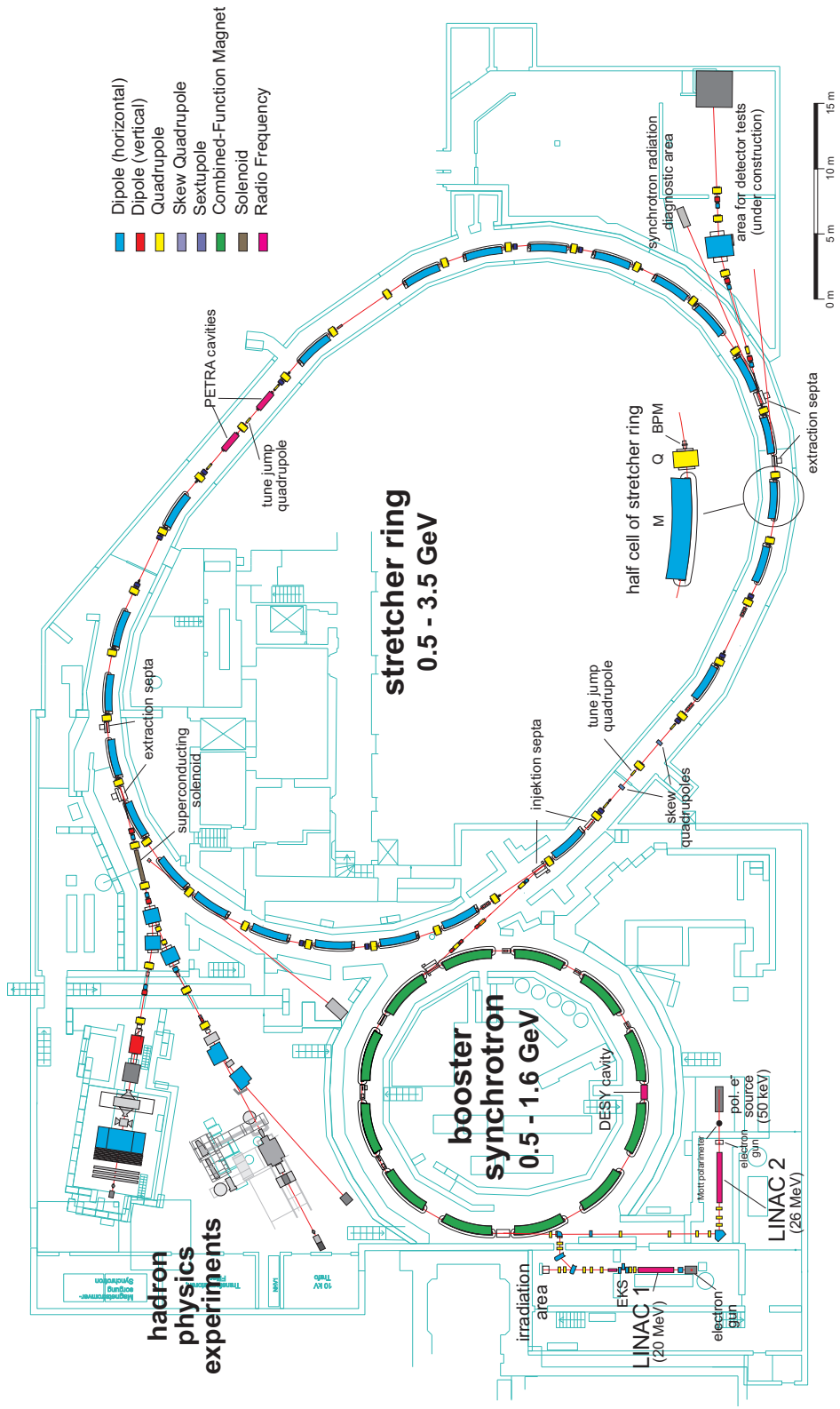


Figure 1.1: Facility drawing of the ELSA accelerator laboratory.

Charged Particle Beam Dynamics In Electron Storage Rings & Imaging Techniques

Due to the fundamentals of electromagnetic theory [JAC98] charged particle deflection causes the emission of electromagnetic radiation. In electron synchrotrons this *synchrotron radiation* occurs intensively when ultra-relativistic particles are deflected in the magnetic dipole fields of the bending magnets. In combination with the accelerator's subsystems – such as the accelerating cavities – this emission process strongly determines the particles' dynamics and hence the beam dimensions. When utilizing the synchrotron radiation, it is important to understand the source point parameters which are given by the underlying physics of the electron beam. The following sections summarize relevant laws and relations. If not stated otherwise, the formulas and context are in accordance to [WIL86].

2.1 Particle Motion

The radiation source point in a bending magnet is solely determined by the electrons' locations in six-dimensional phase space. These coordinates denote unavoidable deviations of an arbitrary real particle from an *ideal particle* traveling on the design orbit. We express these coordinates in vectorial notation:

$$\vec{x}(s) = (x, x', z, z', \Delta s, \delta)^T(s), \quad (2.1)$$

where x and z are the horizontal (radial) and vertical (axial) displacements and x' and z' the corresponding divergences. Δs describes the longitudinal displacement from the design particle and $\delta = \frac{\Delta p}{p} = \frac{\Delta E}{\beta^2 E}$ its momentum deviation. For ultra-relativistic particles we obtain $\frac{\Delta p}{p} \equiv \frac{\Delta E}{E}$ since $\beta \rightarrow 1$. Note that all entries of Eq. (2.1) are dependent on the particle's longitudinal position throughout the lattice. The lattice represents the magnet structure around the ring which determines the beam optics. The coordinate system used for beam tracking in circular machines is of curvilinear and right-handed nature (x, s, z) as illustrated in Fig 2.1.

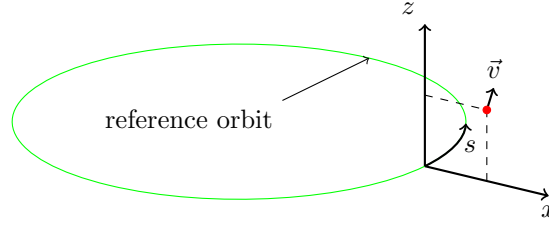


Figure 2.1: Coordinate system used for particle tracking in circular machines.

2.1.1 Transverse Motion

Particle motion is described in linear approximation by *Hill's* differential equations for both transverse planes:

$$x''(s) + \left(\frac{1}{R^2(s)} - k(s) \right) x = \frac{1}{R(s)} \frac{\Delta p}{p} \quad (2.2)$$

$$z''(s) + k(s) z = 0, \quad (2.3)$$

where $R(s)$ is the local bending radius, $k(s)$ the quadrupole strength, p the particle's momentum and Δp its momentum deviation. No coupling between the transverse planes is assumed. Eq. (2.3) holds for a machine where bending takes place solely in the horizontal plane. The solution of Eq. (2.2) yields a single particle trajectory

$$x(s) = \sqrt{\tilde{\epsilon}_x \beta_x(s)} \cos(\psi_x(s) + \phi_x), \quad (2.4)$$

where $\tilde{\epsilon}_x$ is called the *single particle emittance*, $\beta_x(s)$ the horizontal β -function (compare Fig. 2.3), ϕ_x an integration constant and

$$\psi_x(s) = \int_0^s \frac{ds'}{\beta_x(s')} \quad (2.5)$$

the particle's phase. Vertical considerations are obtained in analogy.

In a circular machine it is essential that a particle's displacement and angle must differ from turn to turn for any location (compare with Eq. (2.14)), forming an elliptical trajectory in phase space. The enclosed area is a measure for an invariant called the single particle emittance $\tilde{\epsilon}$, based on *Liouville's theorem* in which an area in phase space is preserved if only conservative forces are applied. Despite non-conservative forces act on the beam in electron synchrotrons, the theorem holds as the beam reaches an equilibrium state (compare with section 2.1.3) and deviations occur on a relatively long time scale compared to the revolution period. Since the covered area within phase space is of elliptical nature, one may describe the single particle emittance $\tilde{\epsilon}_x$ with the so called *Twiss-parameters* $\alpha(s)$, $\beta(s)$ and $\gamma(s)$ as in

$$\tilde{\epsilon}_x = \gamma(s)x^2(s) + 2\alpha(s)x(s)x'(s) + \beta(s)x'^2(s) = A/\pi, \quad (2.6)$$

where A is the enclosed area as illustrated in Fig. 2.2.

In a particle distribution the sizes of the individual particle phase space ellipses differ. It is useful to introduce a statistical type of emittance, called the *beam emittance* ϵ . It is a measure of the beam's size and divergence in one particular plane, corresponding to the statistical distribution of particle's displacements and angles which usually follows a *Gaussian* distribution¹. The variances (σ and σ')

¹ The Gaussian distribution is typical for particles at $\gamma \gg 1$.

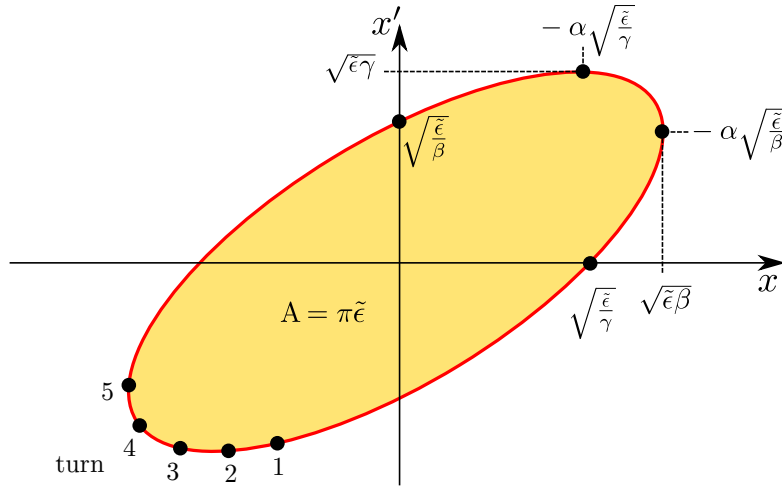


Figure 2.2: Twiss-parameters α , β and γ describing the orientation and size of the phase space ellipse.

also form an ellipse in phase space (e.g. $\{x, x'\}$), thus the beam emittance is derived as

$$\epsilon_x = \sqrt{x^2 \cdot x'^2 - xx'^2} \stackrel{(*)}{=} \sigma_x \cdot \sigma'_x. \quad (2.7)$$

(*) holds if the ellipse's major and minor axis are parallel to the axis of x and x' . Then the beam emittance becomes the product of width and divergence of the corresponding 1- σ distributions. [LEE04, p. 61]

It may now be apparent, that the function $\beta(s)$ is a measure of the envelope enclosing all particle trajectories. It is only dependent on the beam optics² and together with the beam emittance ϵ it defines the 1- σ particle distribution of the beam envelope as in

$$\sigma_x(s) = \sqrt{\epsilon_x \beta_x(s)}. \quad (2.8)$$

The same holds for the vertical plane.

It must be noted that momentum deviation also contributes to the beam size due to sections with dispersion $D(s)$. We obtain an additional displacement Δx for particles with momentum deviation:

$$\Delta x = D(s) \frac{\Delta p}{p}. \quad (2.9)$$

The expected beam size at any location is now depicted by

$$\sigma_x(s) = \sqrt{\epsilon_x \beta_x(s) + \left(D(s) \frac{\Delta p}{p} \right)^2}. \quad (2.10)$$

As will be shown in section 2.1.3, beam emittance ϵ and energy deviation of a particle distribution $\left(\frac{\sigma_E}{E}\right)$ are dependent on the beam energy. Also note that there are no dispersive elements in the vertical plane if the accelerator is built as flat machine such as ELSA.

Dispersion $D(s)$ and both transverse functions $\beta_x(s)$ and $\beta_z(s)$ are illustrated for ELSA in Fig. 2.3. One may notice that $\beta_x(s)$ and $\beta_z(s)$ are never decreased simultaneously. The reason lies in the focusing

² The functions are normalized to beam energy

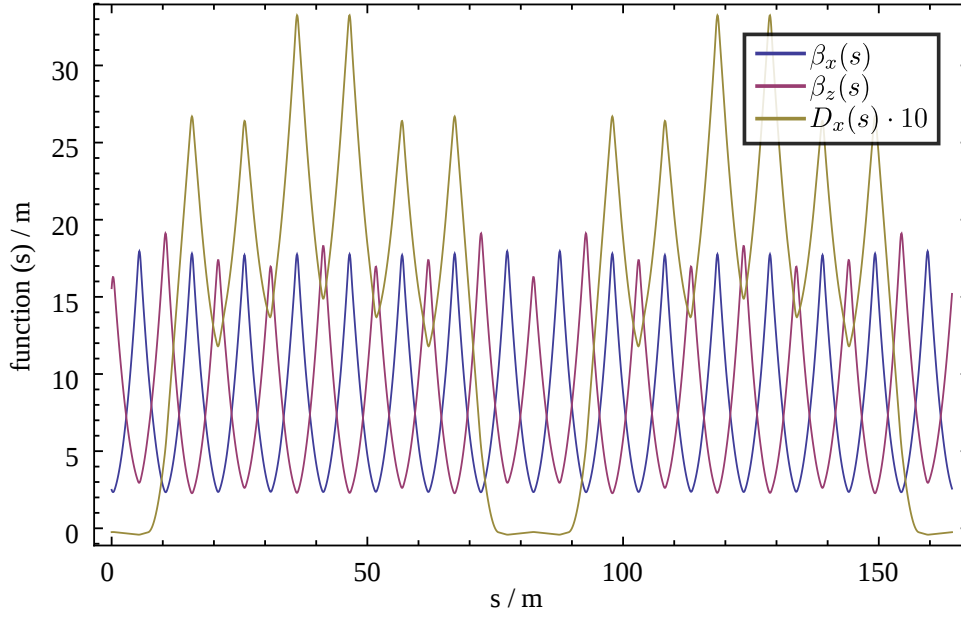


Figure 2.3: Theoretical dispersion $D(s)$ and functions $\beta_x(s)$ and $\beta_z(s)$ throughout the full length of ELSA during the slow extraction process. The tunes are $Q_x = 4.63$ and $Q_z = 4.39$.

properties of magnetic quadrupole fields. If one plane is focused, the other one is defocused. Fortunately overall stability³ is achievable following the optics relation

$$\frac{1}{f_{\text{tot}}} = \frac{1}{f_1} + \frac{1}{f_2} - \frac{d}{f_1 f_2} \stackrel{(*)}{=} \frac{1}{f_1}. \quad (2.11)$$

The equality (*) represents one of many solutions for stability with $d = f_1 = -f_2$. The *thin lens* approximation may be used for short quadrupole lengths L_{quad} . The focal length of a thin quadrupole magnet is then given by

$$f_{\text{quad}} = -\frac{1}{kL_{\text{quad}}}, \quad (2.12)$$

where k is again the quadrupole strength. It is dependent on the gradient of the magnetic quadrupole field. For a conventional iron quadrupole built into ELSA it can for example be calculated by

$$k = \frac{e}{p} \frac{\partial B_z}{\partial x} = \frac{e}{p} \frac{2\mu_0 n I}{a^2}, \quad (2.13)$$

where p is the momentum of the electron with charge e , μ_0 the vacuum permeability, I the current running through the coils with n windings and a denotes the magnet yoke gap distance to the center. The alternating setup of (horizontally) focusing (F) and defocusing (D) quadrupole magnets is called *FODO*. The O denotes zero focusing in between the quadrupoles.

Transverse beam dynamics are dependent on the transverse *tune* of the machine:

$$Q_{x,z} = \frac{1}{2\pi} \cdot \oint \frac{ds}{\beta_{x,z}(s)}. \quad (2.14)$$

³ Focusing in both planes simultaneously

It describes the number of transverse oscillations of an off-orbit particle around the closed orbit within one turn around the accelerator (*betatron oscillation*). In order to obtain a stable beam it is of most importance to set the tune to non-integer, non-half-integer, and so on. This avoids the repetitive effects of magnetic field errors. The phase $\psi_{x,z}$ as denoted in Eq. (2.4) must therefore change non-repetitively from turn to turn. The tune can be shifted via change of quadrupole strength δk according to

$$\Delta Q_{x,z} = \frac{1}{4\pi} \int \beta_{x,z}(s) \delta k_{x,z}(s) ds. \quad (2.15)$$

One therefore expects betatron oscillations with corresponding frequencies

$$\omega_{x,z} = \omega_0 Q_{x,z}, \quad (2.16)$$

where $\omega_0 = 2\pi/T_{\text{rev}} = 2\pi c/L$ denotes the angular revolution frequency, L being the circumference of the accelerator.

Incoherent⁴ betatron oscillations with frequency $\omega_{x,z}$ actually define the transverse dimensions of the beam according to Eq. (2.8). If the beam is kicked transversely at once, one observes a **coherent**⁵ oscillation of the beam at the frequencies denoted in Eq. (2.16). It must be noted that small variations of ω_0 ⁶ result in slightly different oscillation frequencies for the corresponding particles. The common phase of the particles will increasingly differ with time. Therefore a coherent oscillation will always become incoherent. The same holds for longitudinal particle oscillations which are called *synchrotron oscillations*.

2.1.2 Effects of Synchrotron Radiation & Longitudinal Motion

As mentioned in the introduction of this chapter, the emission of synchrotron radiation in combination with the longitudinal electric field of the accelerating cavities $\vec{E}_{\text{el}}(s)$ completely determines the natural beam dynamics and subsequently the beam dimensions. In order to understand this, one must consider the consequences that arise from the emission process. The energy loss of one particle per revolution is denoted as circumference voltage and can be calculated via

$$\Delta E_{\text{SR}}/eV = \frac{e\beta^3}{3\epsilon_0} \cdot \frac{\gamma^4}{R} \approx 88.5 \times 10^3 \frac{(E/\text{GeV})^4}{R/\text{m}}, \quad (2.17)$$

with ϵ_0 being the vacuum permittivity, R the magnet bending radius and $\beta = p/E$ and $\gamma = E/E_0$ the relativistic quantities. The approximation holds for electron synchrotrons. The total power loss due to the emission of synchrotron radiation is consequently

$$\Delta P_{\text{SR loss}} = \Delta E_{\text{SR}} \cdot I_{\text{beam}}, \quad (2.18)$$

where $I_{\text{beam}} = Ne/T_{\text{rev}}$ denotes the stored beam current with N being the total number of particles⁷ in the machine. As consequence the accelerating cavities are operated continuously in order to compensate for synchrotron radiation losses via

$$\Delta E_{\text{SR}} \stackrel{!}{=} \Delta E_{\text{RF}} = \int_{s_0}^s e \left(\vec{E}_{\text{el}}(s) + \vec{c} \times \vec{B} \right) \cdot d\vec{s}. \quad (2.19)$$

⁴ All particle oscillations differ in phase.

⁵ All particles oscillate in phase.

⁶ Due to energy deviation ΔE (see Fig. 2.4).

⁷ assuming charge $Q = Ze = e$ with $Z = 1$ for electrons

ΔE_{RF} represents the particle energy gained from the *Lorentz* force within the RF cavities, \vec{B} is an arbitrary magnetic field. Only the longitudinal component of the electric field \vec{E}_{el} contributes to the scalar product, therefore being the only mechanism available for energy restoration. The sinusoidal electric accelerating field determines the longitudinal spacing of the beam:

$$f_{\text{RF}} = \frac{1}{T_{\text{RF}}} = \frac{c}{\lambda_{\text{RF}}}. \quad (2.20)$$

Electron beams in synchrotrons occur always *bunched*. One obtains as total number of *bunches* in a machine of length L the *harmonic number*

$$h = \frac{L}{\lambda_{\text{RF}}}. \quad (2.21)$$

When ultra-relativistic particles deviate in energy $\Delta E/E > 0$, they become more rigid but the velocity remains unchanged. The additional momentum causes a particle to revolve on a larger orbit compared to the design particle. The revolution period T_{rev} subsequently suffers from time delay and decreases its value of Δs . Longitudinal defocusing occurred. In order to obtain re-focusing the phase ψ_s of the design particle arrival is not coincident with the phase of the maximum cavity voltage U_0 . For relativistic particles ψ_s is located on the falling flank of the sine function as illustrated in Fig. 2.4. The positive phase shift of more rigid particles results in less energy gain when leaving the cavity. This focusing effect results in longitudinal synchrotron oscillations.

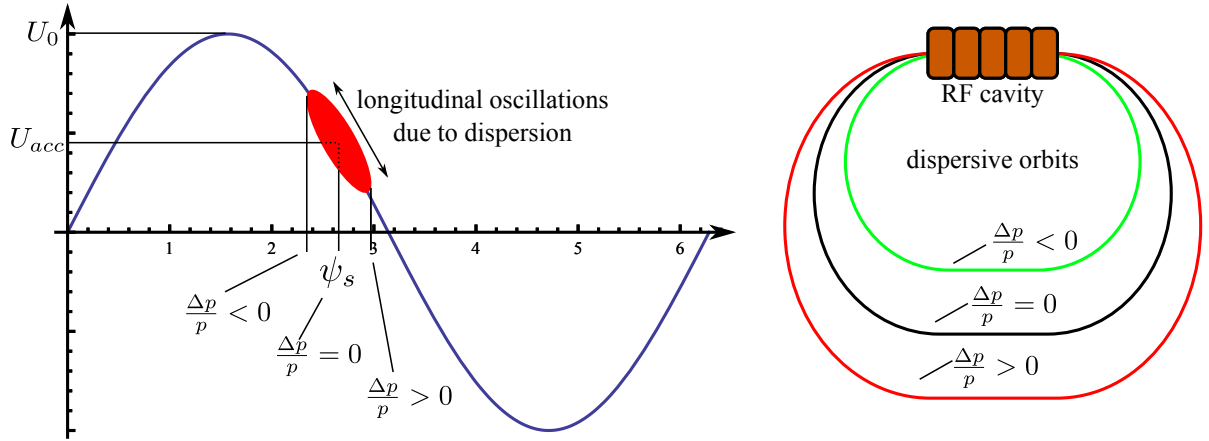


Figure 2.4: Longitudinal incoherent oscillations of the electrons distribution around the synchrotron phase ψ_s at the accelerating voltage U_{acc} . momentum deviation causes particles to propagate on dispersive orbits.

The angular synchrotron frequency ω_s is given by

$$\omega_s = \omega_0 \sqrt{\frac{eU_0 h \alpha_c}{2\pi E}} \sqrt{1 - \frac{1}{q^2}}, \quad (2.22)$$

where E is the particle energy, $q = U_0/U_{\text{acc}}$ the *over voltage* factor of the accelerating cavity and

$$\alpha_c = \frac{\Delta L/L}{\Delta p/p} \quad (2.23)$$

the *momentum compaction* factor. Note the explicit dependency on E keeping energy deviations in mind.

2.1.3 Beam Equilibria & Beam Dimensions

As the emission process of synchrotron radiation is of statistical nature, it *heats* the beam⁸ in all three spacial dimensions. However, due to phase focusing the longitudinal excitation is damped. Since the accelerating cavity restores only the longitudinal momentum component p_{\parallel} , the beam is also damped transversally. The result is an equilibrium state of excitation and damping. If the beam is excited by outer influence for a finite period of time, it will damp back to the equilibrium state with the corresponding damping constant α_i , $i = \{x, z, s\}$ as in

$$\sigma_i(t) = \sigma_{i,0}(1 + e^{-\alpha_i t}). \quad (2.24)$$

The damping constants are obtained via

$$\alpha_i = \frac{\Delta E_{\text{SR}}}{2ET_{\text{rev}}} \cdot J_i, \quad (2.25)$$

where E denotes the beam energy, $T_{\text{rev}} = L/c$ the orbit revolution time and J_i the damping number. The *magnetic structure* parameter \mathcal{D} determines

$$J_s = 2 + \mathcal{D}, \quad (2.26)$$

$$J_x = 1 - \mathcal{D} \quad \text{and} \quad (2.27)$$

$$J_z = 1 \quad \text{with} \quad (2.28)$$

$$\mathcal{D} = \frac{\oint \frac{D_x(s)}{R(s)} \cdot ds}{2\pi R} = \frac{\alpha_c L}{2\pi R}. \quad (2.29)$$

In *separated function machines*⁹ such as ELSA damping occurs in all three planes simultaneously since α_c is small and the damping numbers J_i remain positive.

Naturally, particle distributions have a finite energy deviation σ_E/E . Due to the damping the equilibrium state can be calculated according to

$$\left(\frac{\sigma_E}{E}\right) = \sqrt{\frac{55}{32\sqrt{3}} \cdot \frac{\hbar c \gamma^2}{J_s E_0} \cdot \frac{\langle 1/R^3 \rangle}{\langle 1/R^2 \rangle}} \stackrel{(*)}{=} \gamma \sqrt{\frac{C_q}{J_s R}}, \quad (2.30)$$

where γ is the relativistic quantity, \hbar the *Planck* constant, J_s the longitudinal damping number, R the magnet bending radius and E_0 the rest mass of the corresponding particle. For electrons (*) holds if all bending magnets are equal¹⁰, with $C_q \approx 3.84 \cdot 10^{-13}$ m. Note that the energy deviation rises linearly with beam energy.

In analogy to the betatron oscillations in Eq. (2.16) the incoherent longitudinal oscillations ω_s determine the bunch length σ_s . According to [EBE10] it can be calculated via

$$\sigma_s = \frac{c\alpha_c}{\omega_s} \left(\frac{\sigma_E}{E}\right). \quad (2.31)$$

⁸ increasing incoherent motion of the particle distribution (momentum deviation)

⁹ Focusing magnets and bending magnets are separated.

¹⁰ Bending magnets equal in magnetic field strength and length.

Alternatively one can use the similar relation

$$\sigma_s = \frac{c}{\omega_0} \sqrt{\frac{2\pi\eta E}{heU_0 \cos \psi_s}} \cdot \left(\frac{\sigma_E}{E}\right), \quad (2.32)$$

where $\eta = (1/\gamma - \alpha_c) \approx -\alpha_c$ is the *slippage* factor, h the harmonic number and ψ_s the synchrotron phase. Note the proportionality $\sigma_s \propto \gamma^{3/2}$.

The damping has a similar effect on the horizontal *natural* emittance ϵ_x is in Eq. (2.30). It can be calculated by

$$\epsilon_x = \frac{55}{32\sqrt{3}} \cdot \frac{\hbar c \gamma^2}{J_x E_0} \cdot \frac{\langle 1/R^3 \cdot \mathcal{H}(s) \rangle}{\langle 1/R^2 \rangle}, \quad (2.33)$$

with

$$\mathcal{H}(s) = \gamma(s)D^2(s) + 2\alpha(s) \cdot D(s)D'(s) + \beta(s)D'^2(s). \quad (2.34)$$

Here $\alpha(s)$, $\beta(s)$ and $\gamma(s)$ are again the *Twiss*-parameters (compare Eq. (2.6)) and $D(s)$ the dispersion function. If all bending magnets are equal we obtain for electron beams

$$\epsilon_x[\text{m} \cdot \text{rad}] = 1.47 \cdot 10^{-6} \cdot \frac{E^2[\text{GeV}]}{R[\text{m}] \cdot L[\text{m}]} \cdot \int_0^L \mathcal{H}(s) \cdot ds. \quad (2.35)$$

Note that the natural emittance scales with E^2 . Based on Eq. (2.10) we can conclude that the transverse beam size scales linearly with E .

It should be noted that the emittance is strongly dependent on dispersion as obtained from Eq. (2.34). Dispersion is neglectable in the vertical plane, yet the emittance is not observed experimentally to be infinitely small. Coupling effects between the horizontal and vertical plane due to magnet misalignments contribute to ϵ_z and hence widen the vertical beam size σ_z . The transverse emittances share the relation

$$\epsilon_z = \kappa \epsilon_x, \quad (2.36)$$

where κ is the *emittance coupling* factor.

The above presented quantities are summarized exemplarily in Tab. 2.1 for ELSA.

Table 2.1: ELSA pulse stretcher ring parameters

Parameter (at 3.2 GeV if applicable)	Value
Beam energy E	0.5–3.5 GeV
Circumference L	164.4 m
Lattice type	<i>FODO</i>
Cavity RF frequency f_{RF}	499.67 MHz
Circulation frequency f_{rev}	1.82 MHz
Harmonic number h	274
Momentum compaction α_c	6.3 %
Bending radius R	10.88 m
Energy loss per turn $\Delta E_{\text{SR}}(E)$	0.85 MeV
Natural emittance $\epsilon_x(E)$	0.75 $\mu\text{m rad}$
Natural energy spread $\left(\frac{\sigma_E}{E}\right)(E)$	0.08%
Damping times $\tau_x, \tau_z, \tau_s(E)$	4.9 ms, 4.1 ms, 1.9 ms
Bunch length $\sigma_s(E)$	102 ps
Betatron tunes Q_x and Q_z	4.63, 4.39
Synchrotron frequency f_s	88.0 kHz

2.2 Nature of Synchrotron Radiation

The properties of synchrotron radiation impose certain requirements on an optical transfer beamline. The relevant theoretical fundamentals of synchrotron radiation are briefly presented in this section.

2.2.1 Radial Distribution

Accelerated charged particles at classic velocities v radiate an amount of power according to the *Larmor* formula [WIE95]

$$P = \frac{2}{3} \frac{1}{4\pi\epsilon_0} \frac{e^2 \dot{v}^2}{3c^2}. \quad (2.37)$$

The radial power distribution per solid angle is well known from a classical Hertz dipole. It holds for the rest frame of the electron:

$$\frac{dP}{d\Omega} = \frac{e^2}{16\pi^2\epsilon_0 c^3} \dot{v}^2 \sin^2 \phi. \quad (2.38)$$

ϕ is the angle between the direction of acceleration and the observing point. It is apparent that the power of radiation is proportional to the acceleration \dot{v} which is performed by the bending magnets of particle accelerators. However, in this case the particles are moving at ultra-relativistic velocities. When considering the power distribution in the laboratory frame, it becomes conical and highly collimated into the direction of movement:

$$\frac{dP}{d\Omega} = \frac{e^2 \dot{v}^2}{16\pi^2\epsilon_0 c^3} \frac{1}{(1 - \beta \cos \phi)^3} \left[1 - \frac{\sin^2 \phi \cos^3 \theta}{\gamma^2 (1 - \beta \cos \phi)^2} \right]. \quad (2.39)$$

Here \dot{v} corresponds to $\beta^2 c^2 / R$ as given by the centrifugal force. The power distribution is illustrated in Fig. 2.5.

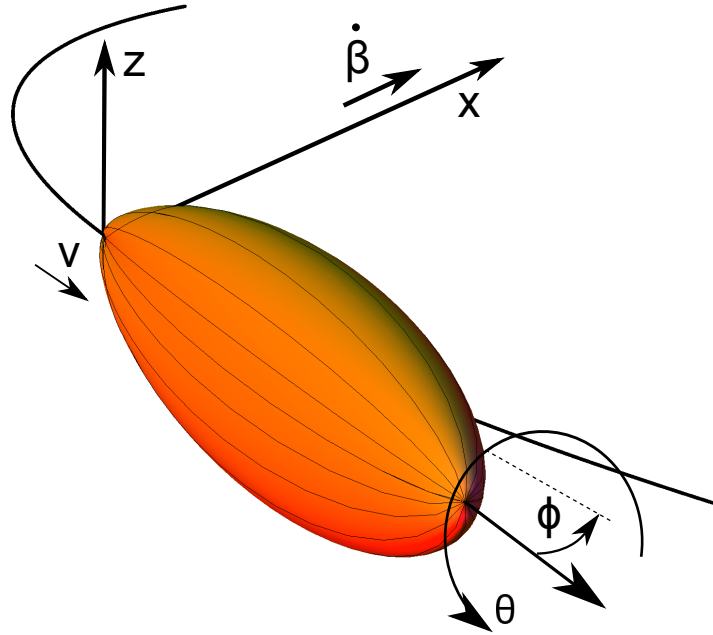


Figure 2.5: Calculation of the angular power distribution as given by Eq. (2.39) at $\beta = 0.9$.

The *root mean square*¹¹ opening angle of the total radiation is given by Eq. (2.39) and corresponds to

$$\phi_{\text{rms}} \approx \frac{1}{\gamma}. \quad (2.40)$$

Synchrotron radiation emitted from ultra-relativistic particles (e.g. $\gamma \approx 6000$) is therefore highly collimated.

2.2.2 Spectral Distribution

One has to keep in mind that the radiation is imaging the *bunched* electron distribution in the machine. As the bunches move across the orbit, the emitted light is swept along the outer vacuum chamber. Due to the $2/\gamma$ collimation, an observer behind a horizontal aperture therefore receives photons emitted between the points P_0 and P_1 . The geometric circumstances are illustrated in Fig. 2.6.

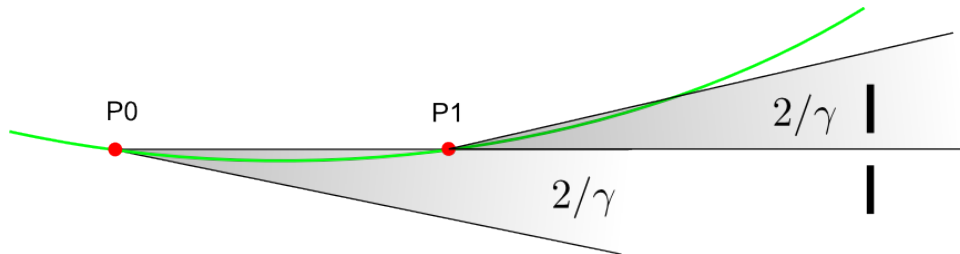


Figure 2.6: An observer sees the emitted light of particles between point P_0 and P_1 .

As consequence the duration of the light pulse δt determines a broad spectrum of emission from a

¹¹ as in $\sigma_{\text{rms}} = \sqrt{\sum_i x_i^2}$

bending magnet. It is given by the difference of travel time of photon and electron as in

$$\delta t = t_e - t_\gamma \approx \frac{4R}{3c\gamma^3}. \quad (2.41)$$

This very short pulse duration translates into an energy uncertainty, due to the uncertainty principle of wave mechanics. It is sufficient to estimate a *critical frequency* ω_c based on half of the signal duration $\frac{1}{2}\delta t$. One obtains an approximation for the critical frequency ω_c according to

$$\hbar\omega_c = \delta E \approx \frac{h}{\delta t} \approx \frac{\hbar 3c\gamma^3}{4R}. \quad (2.42)$$

The spectrum then spans over

$$\omega_{\text{typ}} = 2\omega_c. \quad (2.43)$$

According to [LEE04] the intensity spectrum can be calculated via

$$I(\omega) = \frac{\sqrt{3}e^2}{4\pi\epsilon_0 c} \gamma \int_{\omega/\omega_c}^{\infty} K_{5/3}(y) dy, \quad (2.44)$$

where $K_{5/3}(y)$ is a modified *Bessel* function. The spectrum is visualized in Fig. 2.7 for different electron beam energies.

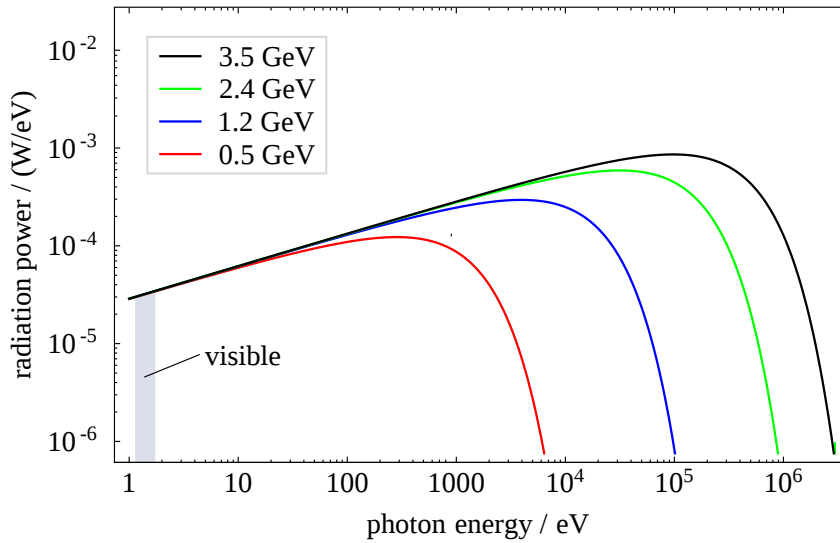


Figure 2.7: Frequency spectrum of the radiated flux for different electron beam energies.

The intensity of the visible part of the spectrum remains unchanged for the available beam energies. However, the high energy components ranging to hard X-rays are of importance considering machine protection.

Focusing on low energy radiation only ($\omega \ll \omega_c$), [WIE95] states a law for the horizontal emission angle which is dependent on the photon energy $\epsilon_{\text{ph}} = \hbar\omega$:

$$\phi_{\text{ph}} \approx \frac{0.54626}{E[\text{GeV}]} \left(\frac{\omega}{\omega_c} \right)^{1/3} = \frac{7.124}{(R[\text{m}]\epsilon_{\text{ph}}[\text{eV}])^{1/3}}. \quad (2.45)$$

2.3 Imaging Techniques

The geometric boundary conditions of a given location imposes certain requirements concerning the set-up of an optical transfer beamline. In good approximation the theory of geometric optics yields sufficient results for macroscopic imaging calculations. Together with the basics of geometric optics, an overview of *microscopic* image broadening effects typical for synchrotron light sources will be discussed briefly in the following section.

2.3.1 Geometric Optics

The divergent photon beam from a point source may be focused by an imaging lens with focal distance f in order to obtain an image of the source. Pure geometric consideration including the *theorem on intersecting lines* yield that the magnification M of an object with dimension¹² G is

$$M = \frac{B}{G} = \frac{b}{g}, \quad (2.46)$$

where B is the size of the image and g and b the distance of the imaging lens to the object and the image. The focal distance f is connected to g and b via

$$\frac{1}{f} = \frac{1}{g} + \frac{1}{b} = \frac{1}{M(g-f)}. \quad (2.47)$$

The right part of the equation is obtained using Eq. (2.46).

If an image with magnification M_1 is imaged again by a system with magnification M_2 and so on, we obtain as total magnification

$$M_{\text{tot}} = \prod_i M_i. \quad (2.48)$$

For example, a regular *Kepler* telescope consists of three convex imaging lenses (including the eye lens of the observer). The ocular lens of the telescope acts as a collimator, relaying parallel light bundles. Therefore the distance of eye and ocular lens can in principle be infinite. One obtains for final magnification at the final image location b_2

$$M_{\text{tot}} = M_1 \cdot M_2 = \frac{f_1}{g_1 - f_1} \cdot \frac{b_2}{g_2} = \frac{f_1}{g_1 - f_1} \cdot \frac{f_3}{f_2}, \quad (2.49)$$

since $b_2 = f_3$ and $g_2 = f_2$.

2.3.2 Transverse & Longitudinal Resolution

Two point sources can be *resolved*, when their images are distinguishable by an observer. In general, images appear **always** broadened due to finite bandwidth of any imaging system. For macroscopic considerations, those effects are somewhat neglectable. For synchrotron radiation observers however, some of the following effects may be of relevance.

¹² Distance from the optical axis.

Depth of field

A longitudinally distributed source such as the curved electron beam within a dipole magnet can only be imaged with a finite depth of field. This means that source points which are located slightly out of the imaging system's focal plane will yet be detected as *circles of confusion*. The effect vanishes with curvature and is also dependent on the photon opening angle. Following [BER06] we find the effect of broadening to be

$$\sigma_{\text{dof}} = \frac{\rho_{\text{max}}}{\sqrt{6}} = R \frac{b}{4g\sqrt{6}} \phi_c (\Delta\phi_x + 2\phi_\gamma), \quad (2.50)$$

where ρ_{max} is the maximum radius of a circle of confusion, R is the magnet bending radius, g and b the distance from source and image, ϕ_x the limiting horizontal aperture, $2\phi_\gamma$ the photon opening angle and ϕ_c the smaller of the two.

Curvature

The curvature of the emission path broadens the beam additionally. Geometric considerations as in [ZAN08] allow the calculation of the broadening magnitude:

$$\sigma_c \approx \frac{1}{2} R \phi_\gamma^2, \quad (2.51)$$

where R is the bending radius and ϕ_γ the photon opening angle.

Diffraction

Fraunhofer diffraction occurs when a light beam propagates through a finite aperture of size D . The broadening is dependent on the wavelength λ and the distance of source and aperture g as in [ZAN08]:

$$\sigma_{\text{diff}} \approx 0.18 \frac{2\lambda g}{D}. \quad (2.52)$$

Note that the slit width decreases the horizontal acceptance and therefore improves the resolution according to depth-of-field and curvature correction. The diffraction effect however counteracts and dominates at low values of D .

Dispersion

One is usually more interested in longitudinal broadening effects that are caused by dispersive media, such as the imaging lenses. The medium specific refractive index $n = c/v$ changes for different wavelengths, accounting for different propagation speeds v through the medium as compared to the speed of light c . The corresponding time delay τ of two initially coincident waves with wavelengths λ_1 and λ_2 after a propagation distance Δs can be calculated according to

$$\tau = \Delta t_{\lambda_1} - \Delta t_{\lambda_2} = \frac{\Delta s}{c} (n(\lambda_1) - n(\lambda_2)). \quad (2.53)$$

2.3.3 Operation Principle of a Streak Camera

Streak cameras resolve picosecond time structures of incident light. The principle of functionality is somewhat similar to that of an oscilloscope and is illustrated in Fig. 2.8.

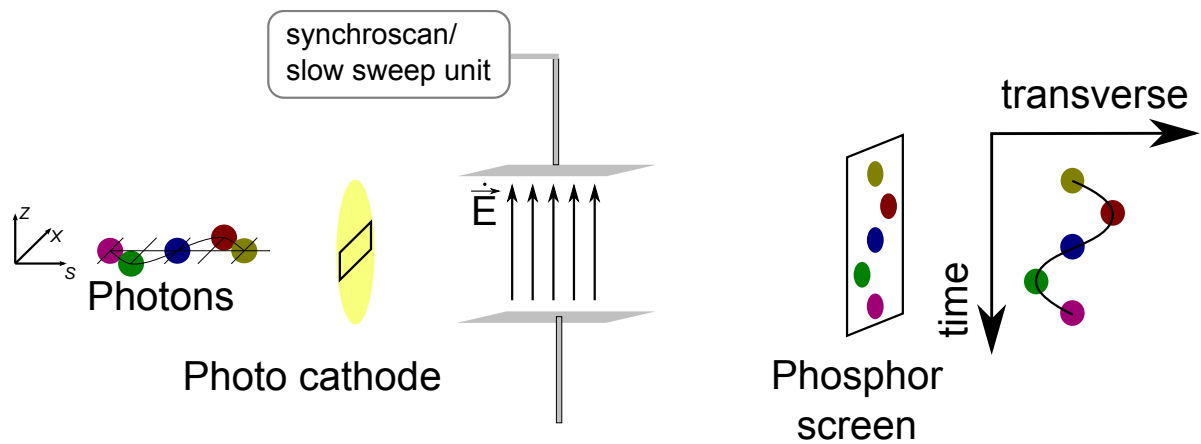


Figure 2.8: Schematic functionality principle of a streak camera.

Incident light emits photo electrons from a photo cathode. The electrons propagate longitudinally and therefore retain the temporal structure of the input signal. A time-dependent electric field \vec{E} deflects the electrons (vertically). The time dependency translates into a difference in height at which the electrons are imaged when illuminating a fluorescent phosphorous screen. Its illumination is captured by a CCD camera in order to obtain a digitized image. Summarized, electron distributions containing the time structure of the incident light are quickly streaked across an imaging screen. The vertical spacial axis now contains temporal information. In order to maximize resolution in the sweep direction, a thin slit always collimates the incident light signal. One therefore loses information of one transverse dimension.

At electron synchrotron facilities, usually two modes of operation are performed in order to obtain beam images:

Slow Sweep

When the deflecting electric field is changed linearly with time ($\dot{\vec{E}} = \text{const}$), one obtains a (vertical) single streak image. These measurements are of interested for transverse beam dynamics. However, the faster the streak, the less intensity is distributed along a unit area. The signal to noise ratio decreases. Low intensity must be compensated by integration. If one is interested in a precise longitudinal measurement in respect to the synchrotron phase ψ_s , good synchronization is granted by another mode of operation.

Synchroscan

The linear ramp of the changing electric field is replaced by a sinusoidal electric field, usually operating at a sub-harmonic of the accelerator's master RF frequency f_{RF} (e.g. $f_{\text{RF}}/4$). This yields precise synchronization with the bunch spacing λ_{RF} and therefore offers good quality measurements of the longitudinal bunch structure in respect to the synchrotron phase ψ_s . At the fourth RF subharmonic, every 4th electron bunch is imaged onto the same spot.

In order to avoid this vertical integration, a horizontal slow sweeping electric field may be applied which separates the signals. A schematic explanation of synchroscan with *dual time base extension* is illustrated in Fig. 2.9. This operation mode combines precise longitudinal measurements with beam dynamics on longer time scales.

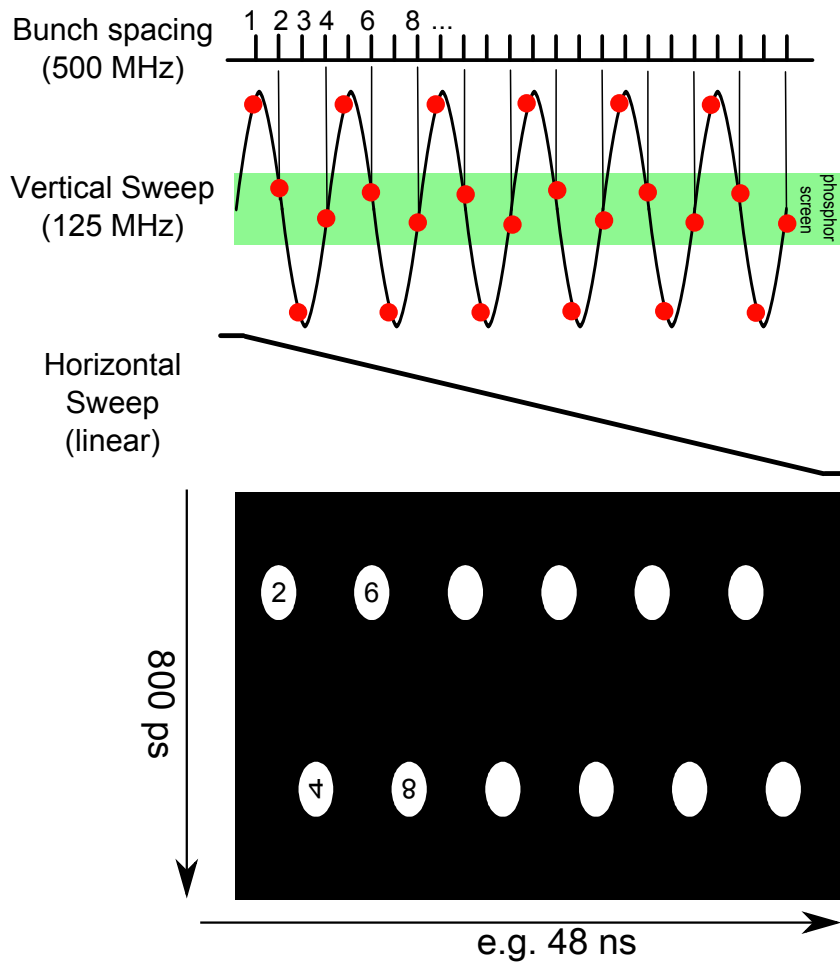


Figure 2.9: Schematic drawing of the synchroscan principle with dual time base extension and typical measurement result. The red dots mark an incident light pulse swept across the phosphorous screen.

It must be noted that operation on the fourth sub-harmonic $f_{RF}/4$ induces a phase jump of the streak images after one lattice revolution, if the harmonic number h is not a multiple of 4. For example: If pulse #1 hits the top flank of the sinusoidal signal, it is not displayed on the phosphorous screen. Pulse #2 is imaged on the falling flank, signal #3 overshoots and the upward streak will be populated by signal #4. After 274 incidents, signal #2 is now illuminating a rising flank and so on. Therefore one expects that upper and lower horizontal image are similar on **long** horizontal time scales (e.g. $\Delta t \geq T_{rev}$).

The M7 Diagnostic Beamline

The set-up of the optical transfer beamline delivering the synchrotron radiation from the source point to the diagnostic devices is described in this chapter. The beamline consists of an evacuated section guiding the synchrotron light out of the accelerator tunnel into an external laboratory and of a *diagnostics section* at atmospheric pressure. Front and back end were designed and installed within the scope of [ZAN13]. The design, set-up and commissioning of the diagnostics section was performed within the scope of this thesis. The following chapter gives an overview of the *experimental setup*.

3.1 The Source Point

The source point for the beamline is determined by the center tangent of the spout pipe adjacent to the M7 dipole vacuum chamber. A drawing is available in appendix A Fig. A.1. Drawing based measurements determine the source point to be $s = (38.53 \pm 0.05)$ m downstream from the injection septum. This also corresponds to a distance of (33.13 ± 0.05) m from the zero-point of the *MAD-X* ELSA model. [FOR02; PRO11] The uncertainty in distance is an estimation comprising unavoidable model, drawing and setup mismatches. In further considerations it will yet be neglected, since a precise misalignment error study of all optical components would exceed the scope of this work. However, the calculated optical values should be considered to be of good proximity to the actual values.

Based on the simulation illustrated in Fig. 2.3 and Fig. 3.1 the corresponding β -functions $\beta_{x,z}(s_0)$ and dispersion value $D_x(s_0)$ are obtained for the source point and summarized in Tab. 3.1. Corresponding to Eq. (2.10), (2.35) and (2.30) the maximum and minimum beam size expected can be calculated for different beam energies. The calculations are given in Tab. 3.2. Note that the emittance coupling factor $\kappa = (7.2 \pm 2.7)$ % was obtained experimentally by [ZAN13] for a beam energy of 1.2 GeV. The calculation assumes the same coupling for other beam energies.

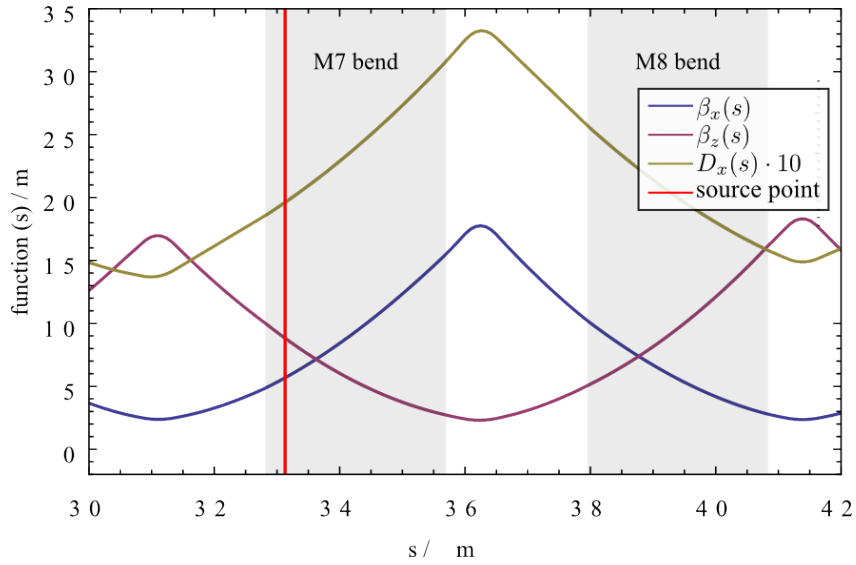


Figure 3.1: $\beta_{x,z}(s)$ and $D_x(s)$ around the source point s_0 of the M7 beamline. The source point is marked in red.

Table 3.1: Source point beam parameters for the M7 diagnostic beamline.

Parameter	Value
$\beta_x(s_0)$ [m]	4.92
$\beta_z(s_0)$ [m]	9.74
$D_x(s_0)$ [m]	1.99

Table 3.2: Expected beam dimensions at the M7 source point for different beam energies E .

E [GeV]	0.5	1.2	3.2
σ_x [mm]	0.39	0.94	2.50
σ_z [mm]	0.11	0.27	0.73
$\sigma_{s,\tau}$ [ps]	14.3	34.3	91.4
$\frac{\sigma E}{E}$ [%]	0.13	0.03	0.08
ϵ_x [nm rad]	18.4	106	752
ϵ_z [nm rad]	1.3	7.6	54.2

In order to observe transverse dynamics the final magnification M_{tot} of the beamline should be chosen to achieve observation of a $10\text{-}\sigma$ distribution. Depending on the observable a variable set of magnification is desirable.

3.2 The Photon Beamline

The 12 m long evacuated beamline guides the synchrotron light from the vacuum chamber of the stretcher ring through the concrete shielding of the accelerator tunnel into an external laboratory. The slit system and primary deflecting mirror are the most relevant components concerning the image properties.

The Beamline Aperture

An aperture defining slit system is positioned 2827 mm downstream from the source point. The slit widths Δx and Δz define angular acceptances as in

$$\Delta\phi_x = \frac{\Delta x/2}{d}. \quad (3.1)$$

The variable rectangular aperture is currently set to $\Delta x = 9$ mm and $\Delta z = 3$ mm. The corresponding angular acceptances from the slit are therefore

$$\Delta\phi_x = 3.2 \text{ mrad}, \quad \Delta\phi_z = 1.1 \text{ mrad}.$$

Using Eq. (2.45) one obtains for some relevant wavelengths the horizontal emission angles as listed in Tab. 3.3.

Table 3.3: Horizontal photon emission angles.

λ_{ph} [nm]	ϵ_{ph} [eV]	ϕ_{ph} [mrad]
700	1.77	2.66
400	3.10	2.20
217	5.72	1.80

We may conclude, that all emission angles are within the acceptance of the slit system.

It must be noted that during the current state of beamline development another aperture further downstream is limiting the horizontal acceptance. A 2" ≈ 25.4 mm wide mirror located at $d = 12.37$ m distance from the source point is tilted by 45° , providing an aperture of $\Delta x = 25.4 \text{ mm} / \sqrt{2} \approx 17.5$ mm (compare with Fig. 3.2). It is located 12.37 m away from the source point. The corresponding acceptances are therefore

$$\Delta\phi_x = 1.4 \text{ mrad}, \quad \Delta\phi_z = 1.1 \text{ mrad}. \quad (3.2)$$

The non-rectangular shape of the mirror narrows the acceptance even more. However, the measurement results (see chapter 4) do not indicate any issues due to this circumstance, as transverse streak camera images are more of qualitative character.

In order to get a feeling for the broadening effects, the contributions are listed for the center wavelength $\lambda = 400$ nm in Tab. 3.4 according to Eq. (2.50), (2.51) and (2.52). Note that the values scale with magnification M_{tot} .

The close distance of the slit system's aperture to the source point and its narrow vertical slit width cause a large amount of vertical diffraction contribution.

Table 3.4: Magnitude of broadening at $\lambda = 400$ nm.

Effect	x	z
σ_{dof} [μm]	6.5	6.5
σ_{c} [μm]	26.3	—
σ_{dif} [μm]	45	136

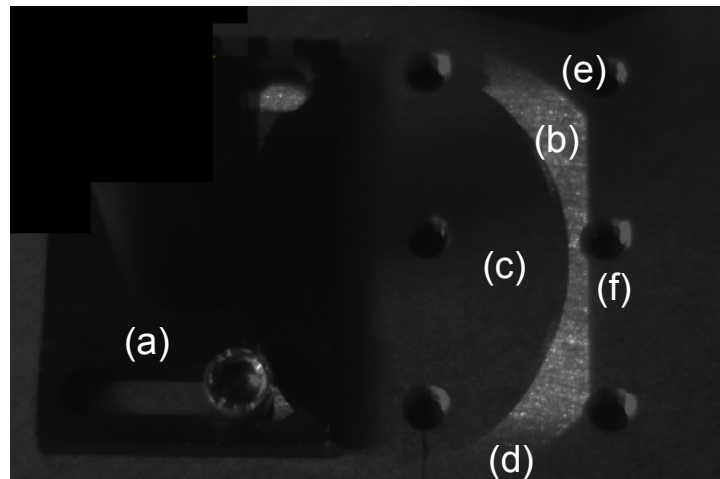


Figure 3.2: Photograph taken downwards onto the base plate (a) of the secondary deflecting mirror during illumination. The mirror aperture is smaller than the dimension of the light bundle, thus stray light (b) and the mirror's elliptical shadow (c) are clearly visible. The vertical aperture is defined by the slit system, as the blurry edges at top and bottom (d) indicate. Yet another aperture seems to cut off horizontal parts of the light. (e) may be an image of the round beam pipe of the vertical chicane. The flat edge (f) may be caused by the finite width of the primary deflecting mirror.

The Primary Reflecting Mirror

The most fragile element of the beamline is the symmetric primary mirror deflecting the low energy light components out of the accelerator plane. The mirror absorbs most of the synchrotron radiation's energy, therefore a rear sided water cooling system suppresses the increase of the mirror temperature. The balance of heating deformation and water pressure was well studied in [HAE11] in order to preserve excellent reflecting properties. Good vacuum ($\approx 10^{-10}$ mbar) protects the mirror surface from blackening due to reactions of the synchrotron light with residual gas molecules [SOL82]. Three ion getter pumps (IGP) along the beamline and a non-evaporable getter pump (NEG) ensure a sufficient suction capacity. The M7 beamline is illustrated in Fig. 3.3.

3.3 Diagnostics Section

The low energy synchrotron light exits the vacuum system vertically through a fused silica glass window and enters an optically sealed box. Its ground plate is a 150×60 cm² large optical table. All diagnostic equipment and the corresponding optics are located here. Two streak camera properties determine the requirements of the beamline:

1. A streak camera is quite light sensitive in certain modes of operation. On the other hand, some modes require maximum achievable illumination.
2. Its active photo cathode has a size of only 0.15×4.42 mm². A slit system usually reduces this area additionally. One transverse dimension is always cut off.

Therefore the optical transfer beamline has to provide

- precise beam positioning capabilities for centered slit illumination,

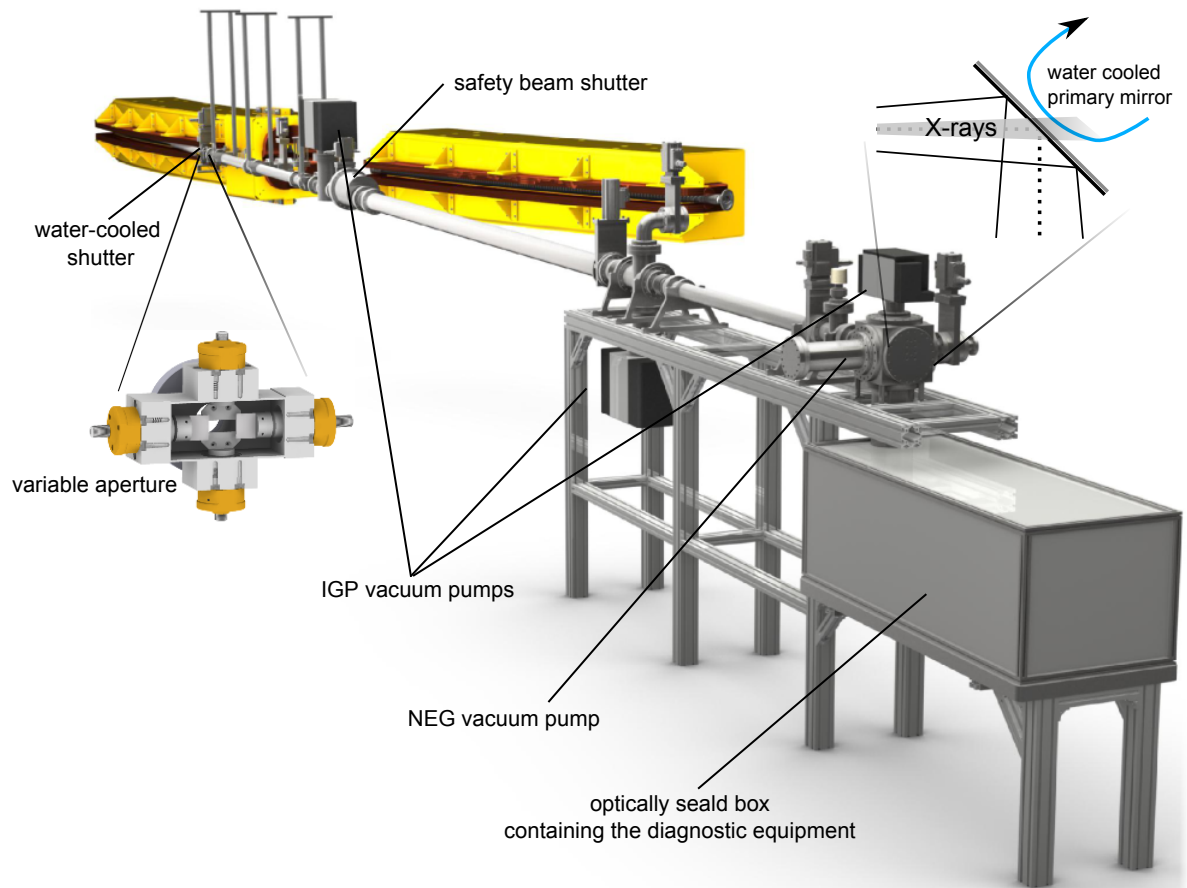


Figure 3.3: Overview of the M7 diagnostics beamline. An adjustable rectangular aperture is located ≈ 3 m downstream from the source point. The long beam pipe ensures a pressure gradient providing an ultra-high vacuum at the primary reflecting mirror at the end of the pipe. The synchrotron light exits the vacuum vertically through a fused silica glass window and enters an optically sealed box.

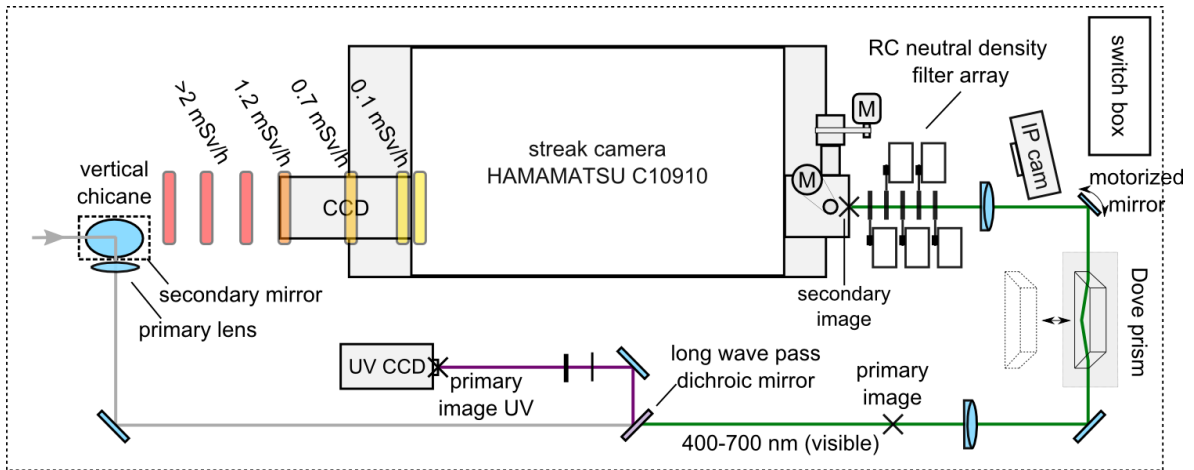


Figure 3.4: Optics layout close to scale. A dichroic mirror separates the UV from visible synchrotron light. The broad band visible light is magnified, rotated and attenuated before being guided onto the streak camera's input optics.

- proper image magnification accounting for the finite slit width,
- variable attenuation for machine protection purposes,
- modification of the transverse beam orientation and
- remote control capabilities where required.

The latter arises from the circumstance, that the beamline back-end is located in a radiologically controlled area with no or limited access during machine operation. The assembly providing these requirements is illustrated close to scale in Fig. 3.4. The design has been inspired by [BER06]. However, the boundary conditions at ELSA are unique. A custom solution had to be designed within the scope of this thesis. The path of light is as follows:

A secondary mirror (of 2" diameter, compare with section 3.2) reflects the beam sideways into the optical plane (160 mm above the table's surface). The side reflection causes an image rotation by 90° . A primary focusing lens with focal length $f_1 = 1000$ m ($\lambda = 530$ nm) is located right after the secondary reflecting mirror at $g \approx 12.38$ m away from the source point. A tertiary reflecting mirror then reflects the beam parallel to the long edge of the table. Broad band mirrors and lenses ensure maximum reflection or transmission for the bandwidth of 200–700 nm.

UV camera

A CCD camera sensitive to the UV spectrum is used as beam position monitor. It measures the transverse beam size and is operated in the UV region because of two reasons. According to Eq. (2.52) the image broadening by diffraction is minimized. Secondly, the streak camera's photo cathode response is low at higher beam energies (compare with appendix A Fig. A.2). Withdrawn UV intensities from the main light bundle should remain unnoticed. Therefore the UV components are separated by a *long wave pass dichroic mirror* and reflected sideways. They are then filtered by a bandpass ($\lambda = 217 \pm 10$ nm) and attenuated by neutral density filters. The camera is located at distance $b \approx 1080$ mm downstream from the primary lens. Its focal length is slightly shorter than stated for the center wavelength. The magnification ratio is therefore $M_1 = b/g \approx 0.087$. The camera's frame rate is limited to ≈ 16 Hz providing a time resolution of 63 ms. Its performance is documented in [ZAN13].

Magnifying Telescope

The first real image of the visible light is formed by the primary focusing lens at $b_1 \approx 1090$ mm yielding a magnification of $M_1 \approx 0.088$. A second lens ($g_2 = f_2 \approx 100$ mm) collimates the beam. The collimation yields an extra degree of freedom for the positioning of optical systems further downstream. Due to the parallel light bundles, the distance between lenses 2 & 3 is free to choose. The secondary image is formed by the third lens at a distance $b_2 = f_3 \approx 200$ mm. The total magnification according to Eq. (2.49) is currently set to

$$M_{\text{tot}} = M_1 \frac{f_3}{f_2} \approx 0.176. \quad (3.3)$$

Comparing with Tab. 3.2, M_{tot} satisfies the 10- σ condition for the largest beam size $\sigma_x(3.2 \text{ GeV}) \approx 2.5 \text{ mm}^1$ since

$$10 \cdot M_{\text{tot}} \cdot \sigma_x(3.2 \text{ GeV}) \approx 4.4 \leq 4.42 \text{ mm} = \Delta x_{\text{SC,max}}, \quad (3.4)$$

where $\Delta x_{\text{SC,max}}$ is the maximum photo cathode width of the streak camera.

Orientating Dove Prism

In order to obtain streak camera images of both transverse planes a Dove prism tilted by 45° can be inserted into the beam. It rotates the image by 90° . The mechanism of rotation is the same as performed by the sideways beam deflection in the vertical chicane. The beam is deflected partially upwards and encounters total inner reflection on the tilted long side. The beam is then coupled out of the prism and proceeds its original path². The prism is mounted onto a motorized linear stage allowing remote controlled insertion into the beam path.

Remote Controlled Attenuation and Adjustment

In order to illuminate the small photo cathode of the streak camera, careful beam adjustment must be granted. Unavoidable optics misalignments require remote controlled fine tuning. Since motorized equipment is of great expense only the most crucial components are remote controllable. Those include

- the two axis of the last mirror for *aiming*,
- four motorized linear stages for position fine tuning,
- five motorized filter flippers for a variable combination of attenuation and
- two stepper motors controlling the streak camera slits.

The motor controllers are connected to the PLC³ located in the vicinity of the M7 beamline back-end. Motor control is granted by the ELSA control system. A *switch box* distributes the signals locally to the different motors.

An additional observation camera films the front of the streak camera in order to provide aiming feedback to the user.

Crucial for streak camera operation is a set of varying neutral density filters. Attenuation in the range from OD⁴ $\tau=0-6$ should be available. This is granted by a set of remote controlled motorized

¹ Currently maximum beam energy at ELSA is 3.2 GeV.

² When properly adjusted.

³ Programmable logic controller

⁴ Optical density as in 10^τ being the factor of attenuation.

filter flippers [THOc]. Currently five flippers with attenuation $\tau = 3, 2, 1, 0.5$ and a bandpass filter at $\lambda = (480 \pm 40)$ nm are installed.

Radiation Levels

Radiation surveys⁵ revealed that the left side of the optical table (source point orientated) is encountering high levels of radiation >2 mSv/h (compare with Fig. 3.4). The sensitive CCD camera at the back-end of the streak camera had therefore be protected by locating the streak camera closer to the center of the optical table where radiation decreases. The current location compromises machine protection and available space at the streak camera's front.

A photograph of the set-up is given in Fig. 3.5.

3.4 The Streak Camera System

The streak camera available is the *all-purpose* model C10910 by Hamamatsu. It is expected to provide a time resolution below 1 ps FWHM⁶. [HAM] It offers the option of locating its control computer more than 100 m away from the camera system. The necessity is given by the seclusion of the laboratory and its status as radiologically controlled area. The bridging occurs via fibre cables and corresponding patch panels for USB, FireWire and Ethernet signals.

The analysis of beam dynamics is possible for a wide range of adjustable time windows which become available due to three separate sweeping units.

The synchroscan unit M10911-01 resolves single bunches in time windows from 1.37 ns to 73.4 ps and allows studies of longitudinal coherent beam dynamics as well as single bunch charge distributions. It is operated at 1/4 of the 499.67 MHz cavity RF and therefore displays either even or odd bunches depending on the set delay of the synchroscan signal. The delay can be set by the *high stability delay unit* C12270. It stabilizes the synchroscan frequency phase based on an active feedback loop. This is supposed to suppresses e.g. thermal signal drifts.

The dual time base extender unit M10916-01 performs linear sweeps along the second screen axis in order to separate the bunch sequences. Time intervals available range from 60 ns to 100 ms and allow sectional studies of the 548 ns long bunch train as well as studies of beam behavior over multiple turns. The sweep repetition is limited to 10 Hz. Image sampling over multiple cycles therefore requires good synchronization with the RF signal and the 1.82 MHz ring orbit clock. In order to avoid the phase shift mentioned in section 2.3.3, the trigger signal for the horizontal sweep corresponds to half of the orbit clock: 0.98 MHz. Also, any other trigger can be applied that is synchronized to a certain event. The timing is performed by a DG645 delay generator.

The synchroscan unit can be exchanged with a linear slow sweep unit M10913-01, thus displaying the continuous bunch train on time scales from 1.2 ns to 1 ms. This allows the study of beam dynamics in both transverse planes.

The available time ranges are summarized in Tab. 3.5. A block diagram displaying the streak camera's subsystems is given in Fig. 3.6. The streak camera system can be operated from a terminal in the ELSA control room.

⁵ Photons with $\epsilon_{ph} > 14$ keV are detected.

⁶ Full width at half maximum

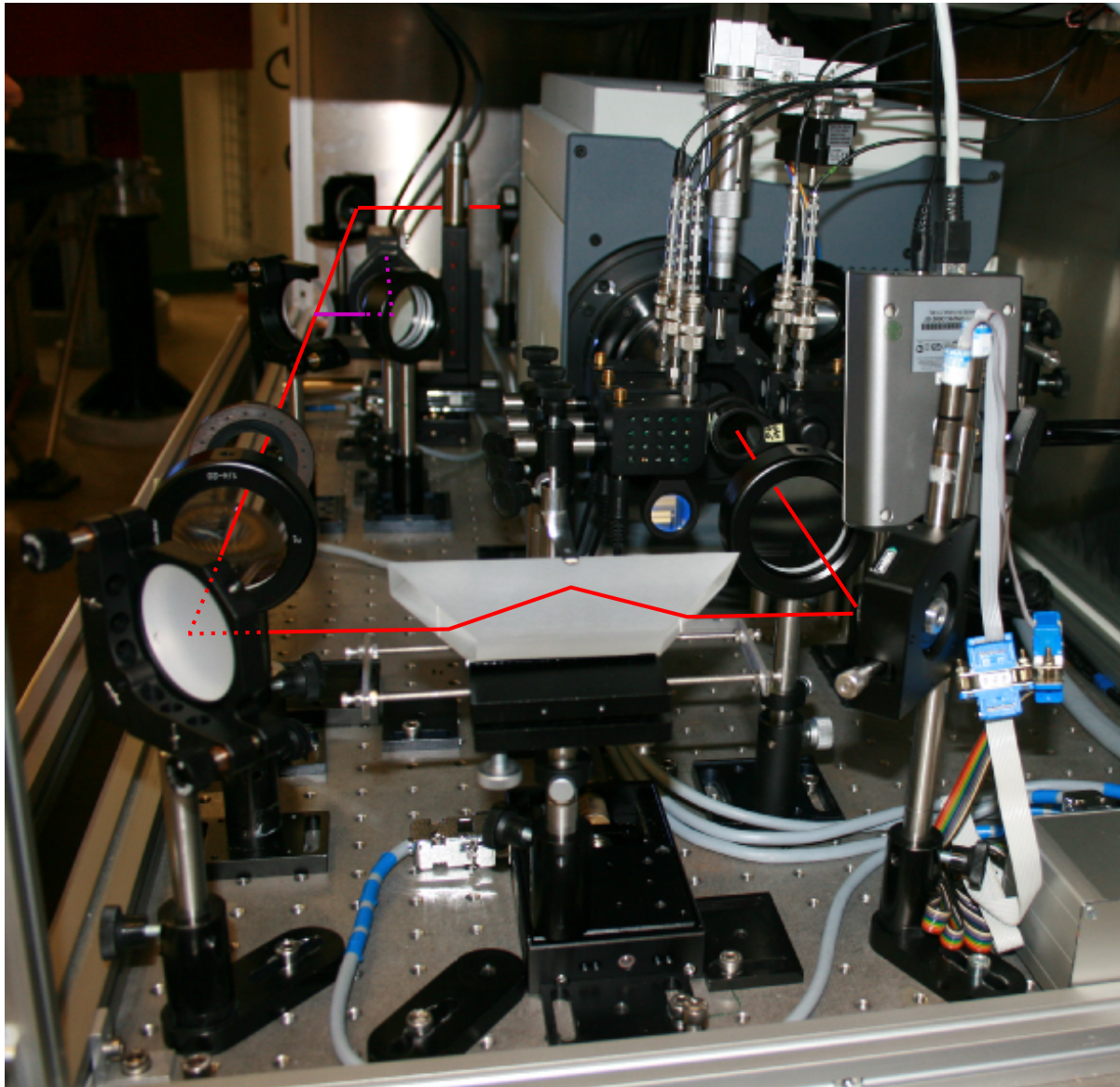


Figure 3.5: Photograph of the M7 beamline diagnostic section. The light path is visualized for broad band (red) and narrow band UV light (purple).

Table 3.5: Available sweep units with corresponding time scales and purpose.

Sweep Unit	Sweep Range	Field of Study
Synchroscan	73.4 ps – 1.37 ns	Charge distribution
Dual time base	59.7 ns – 103 ms	Long. dynamics
Slow Sweep	1.31 ns – 1.02 ms	Transv. instabilities

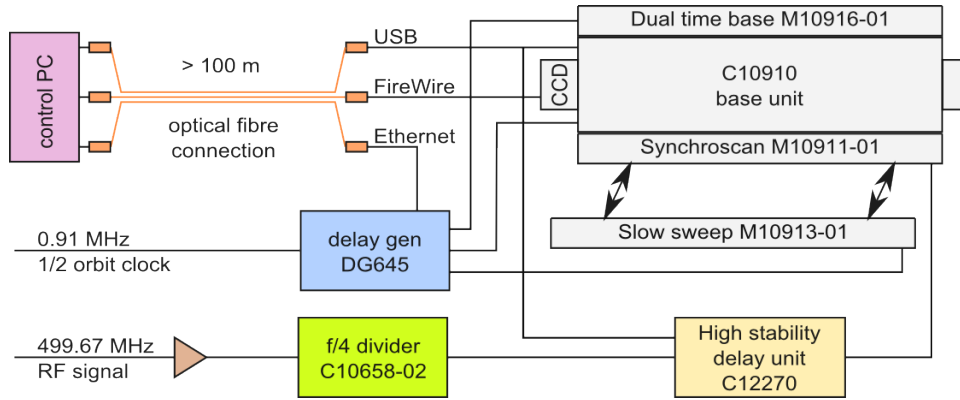


Figure 3.6: Streak camera block diagram.

Measurements

The performance of the streak camera system is demonstrated in this chapter. Selected measurements illustrate beam structure and dynamics under varying circumstances and at different time scales. The measurements were taken during machine development shifts. They do not represent normal operation. Some predictions by the principles of accelerator physics from chapter 2 are demonstrated and verified.

4.1 Slow Sweep

The slow sweep unit is used to obtain information about the macroscopic and microscopic bunch train structure. Time scales available range from 2 ns to 1 ms. However, intensity and synchronization meet their limits at the lower end. Note that the vertical axis corresponds to the time range and the horizontal axis to the *pixel* number of the CCD camera.

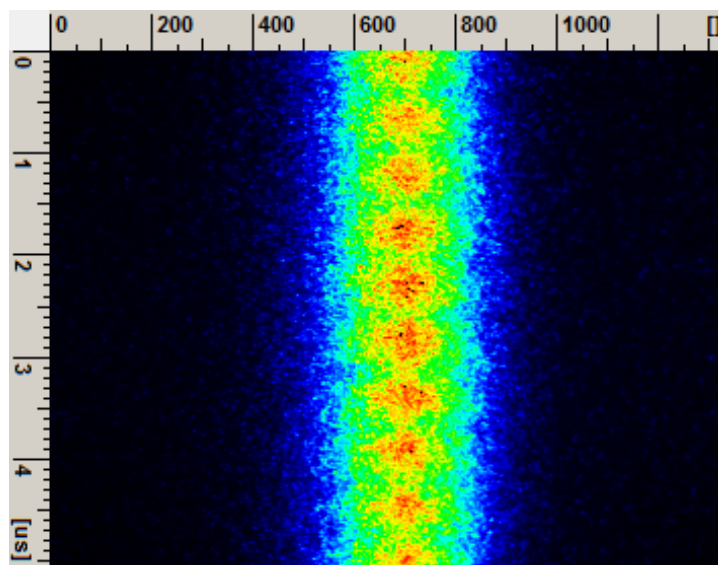


Figure 4.1: Slow sweep across 5 μ s: Top view of a slightly inhomogeneous filling pattern of 10 bunch trains.

Figure. 4.1 displays a 5 μ s sweep. Since $T_{\text{rev}} = 548$ ns, this corresponds to $\approx 10 \times 274$ bunches or

10 *bunch trains*. This *top view* of the beam illustrates a slight macroscopic inhomogeneity of the charge distribution. Since maximum beam homogeneity is desired during normal operation, streak camera observations may be used to fine tune the injection procedure.

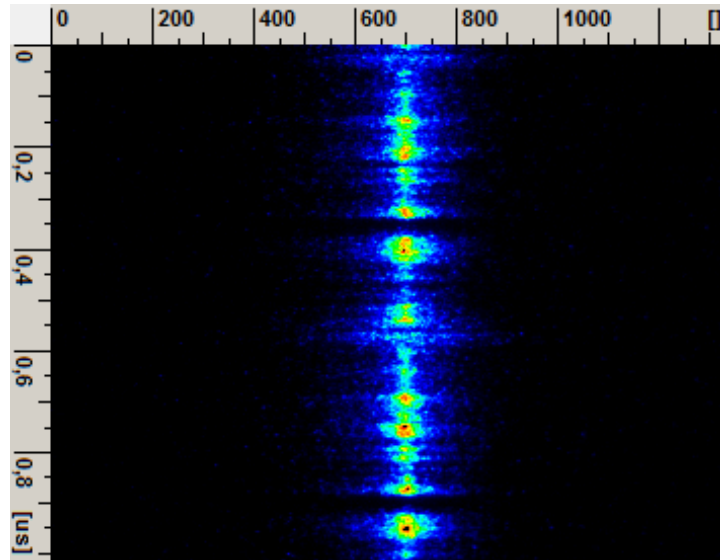


Figure 4.2: Slow sweep across 1 μ s: The beam was distorted by the RF system, the repetitive filling gap is clearly visible.

At 1 μ s one can clearly see the repeating bunch train pattern in Fig. 4.2. The image was taken after the beam was distorted by the RF system.

At a time window of 100 ns, the bunched beam structure becomes visible. Figure 4.3 displays a side view

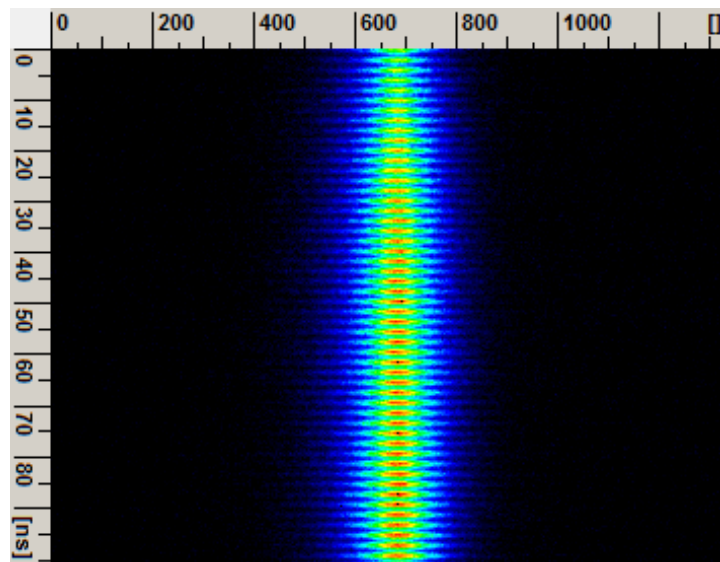


Figure 4.3: Slow sweep across 100 ns: The fine structure of the beam is visible (side view).

As the time window decreases the signal to noise ratio increases. Non-integrated single shot images

meet their limits at time windows around 20 ns. The bunches are clearly visible in Fig. 4.4 and 4.5, yet the transverse dimensions can only be estimated. The centroid seems to be slightly displaced in both images. One may suspect a vertical sinusoidal sequence. However, a single shot image does not reveal any information about the phase relation. Note that the difference in background noise results from different CCD integration times.

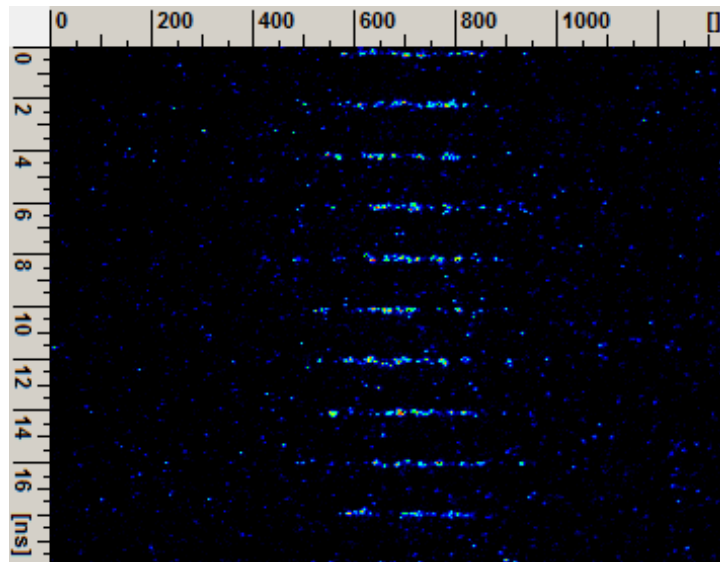


Figure 4.4: Slow sweep across 200 ns: Single shot image of horizontal beam displacements.

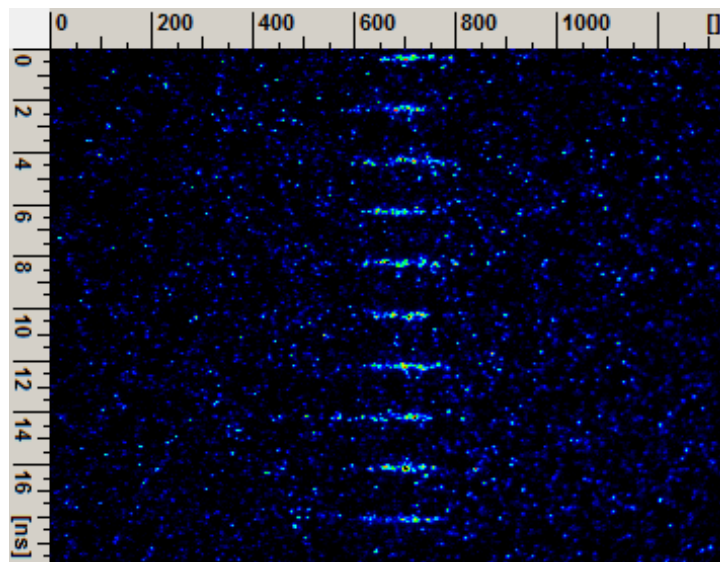


Figure 4.5: Slow sweep across 20 ns: Single shot image of vertical beam displacements.

4.2 Synchroscan

The synchroscan unit is capable of resolving single bunches and is synchronized to the master RF signal. It provides two time scales: The sinusoidal electric field sweeps vertically, thus providing time windows

from 600–1200 ps. A slower horizontal sweep separates the bunch signals in time windows from 60 ns to 100 ms. Note that only the smallest horizontal time ranges display the signals separately as shown in Fig. 4.6.

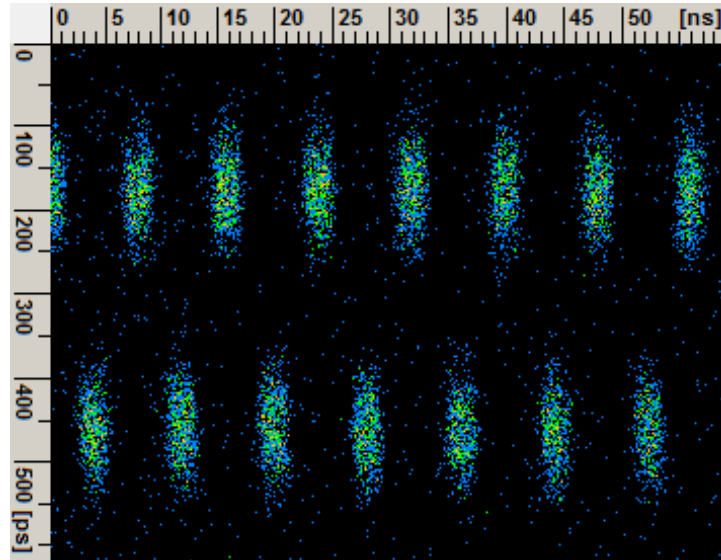


Figure 4.6: Synchroscan across 60ns: Resolution of single bunches. Note that the image was integrated over several turns in order to obtain a decent signal to noise ratio.

4.2.1 Bunch Length & Longitudinal Phase

The bunch length dependency on beam energy E is described by Eq. (2.32) and (2.31). If the synchrotron frequency ω_s is actively kept constant, one expects a linear dependency of bunch length and energy. This measurement and the theoretical calculation is shown in Fig. 4.7.

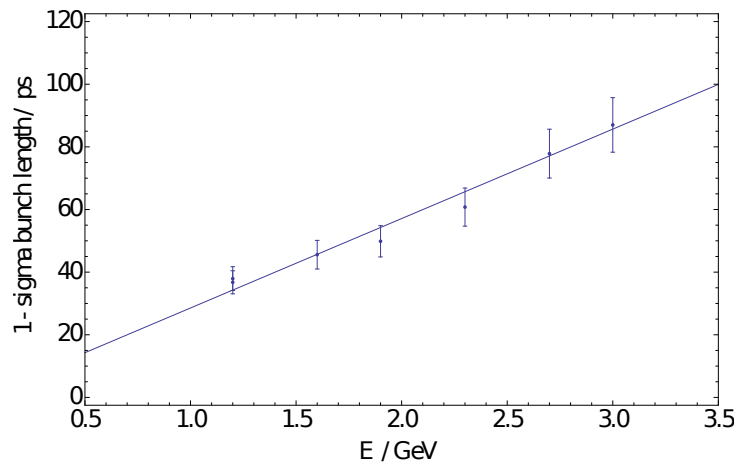


Figure 4.7: The bunch length σ_s increases linearly with energy when ω_s is kept constant. The solid line marks the calculated bunch length for $f_s = 88$ kHz.

The synchrotron frequency was kept at $f_s = 88$ kHz by adjusting the cavity voltage U_0 . The measure-

ment tolerance corresponds to the statistical variation of the images as e.g. observable in the first 10 ms of the image shown in Fig. 4.10. The difference of intensity is yet not understood, but clearly has an effect on the measured bunch length value.

The two nodes at 1.2 GeV (Fig. 4.7) correspond to a measurement with and without the bandpass filter at $\lambda = (480 \pm 40)$ nm inserted. A small amount of broadening may be visible. However, the statistical uncertainty dominates the difference. The Dove prism was not inserted, thus hinting that generic dispersion is yet of low relevance even at short bunch lengths. A slight misalignment of the Dove prism at the time of measurement prevented a direct comparison when moved in. Yet an example: The dove prism is made of N-BK7 glass [THOd]. Refractive indices of interest are e.g. $n(\lambda = 643.8 \text{ nm}) = 1.515$ and $n(\lambda = 404.7 \text{ nm}) = 1.530$. [Sch] According to Eq. (2.53) the time difference τ is thus for a propagation distance of $\Delta s = 9 \text{ cm}$ $\tau = 4.5 \text{ ps}$. It should therefore be of small but noticeable effect when the prism is inserted.

Another bunch length measurement was performed when the cavity voltage U_0 was kept at a constant level. The synchroscan measurement is shown in Fig. 4.8. Note that no dual time base extension unit was used in order to receive maximum spot illumination. This was the first bunch length measurement performed and at the time no optical focusing elements were yet installed.

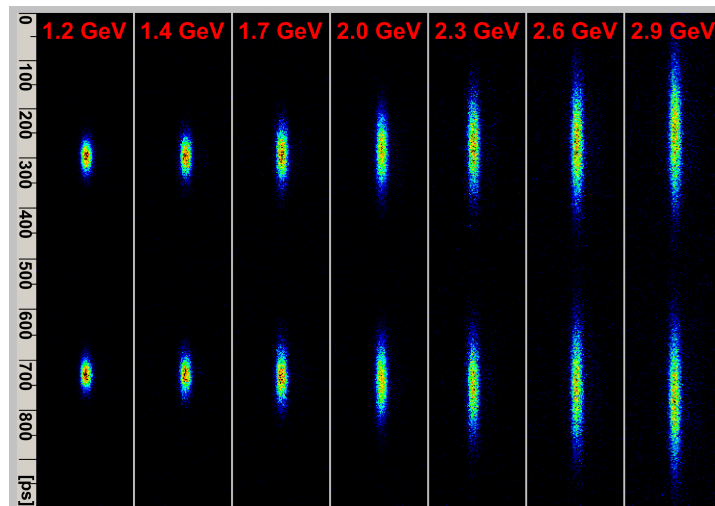


Figure 4.8: Bunch length and phase dependency on beam energy with constant cavity voltage U_0 .

One clearly observes a phase shift of the bunch centroid which corresponds to longitudinal focusing. As the the magnetic field of the bending magnets is increased synchronously with the design energy¹, momentum compaction decreases the phase of arrival at the accelerating cavity. Hence, the electrons interact with a higher electric field strength $E_{el,RF}$ (compare with Eq. (2.19)). Bunch length and phase calculations are compared in Fig. 4.9.

¹ Hence the machine is named *synchrotron*.

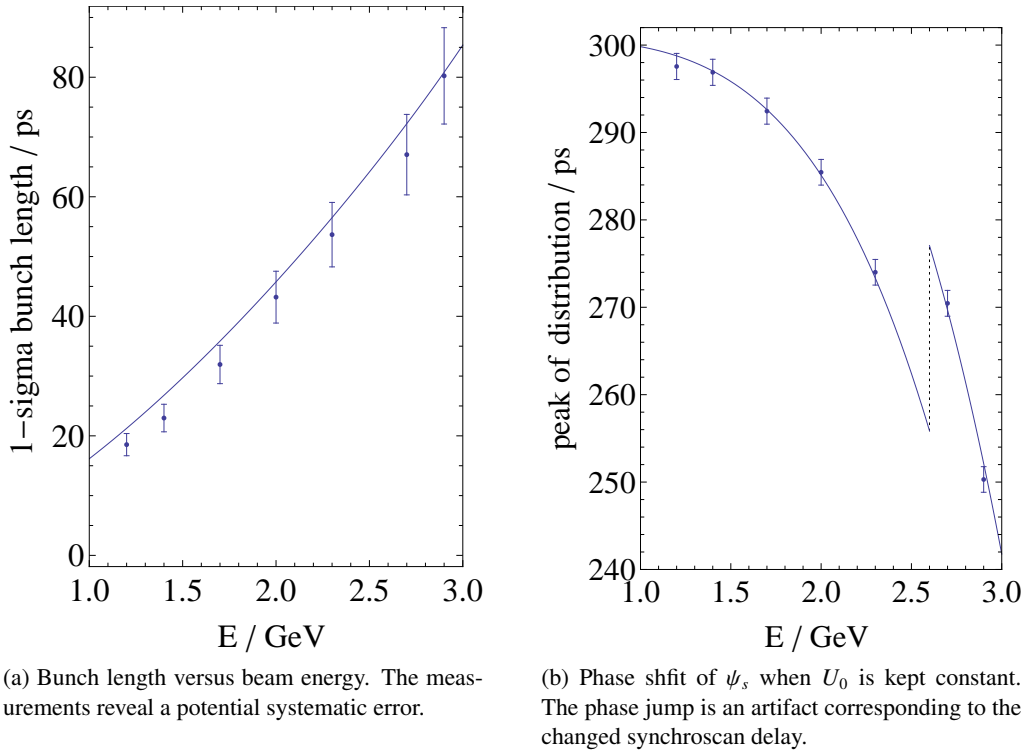


Figure 4.9: The dependency of bunch length and phase shift on beam energy matches the expected values.

It is noticeable, that the measured bunch length seems systematically smaller than the expected value. This may be an artifact caused by the measurement method: An area of interest is spanned across the desired distribution and all contributing rows are horizontally integrated in order to obtain a vertical distribution function. If the distribution is non-uniform, the centroid of a Gaussian distribution is expected to be more populated than the wings. The standard deviation seems decreased.

4.2.2 Grow-Damp-Measurements

A set of measurements was performed where the bunch-by-bunch feedback system [ROT12] was switched off for 5 ms. The horizontal sweeping unit of the streak camera shared the same trigger pulse and therefore was able to capture the arising longitudinal instabilities.

Figure 4.10 is an excellent example of how coherent oscillations transform into incoherent oscillations. The feedback is switched off at ≈ 28 ms and an immediate coherent longitudinal oscillation starts to grow. This is indicated by the rising and falling blue lines. Here, statistically seen, the extreme flanks of the sinusoidal oscillation are most *populated*. This becomes clear when remembering that the derivative of a sine function is lowest at the extremes and highest at the zero crossing. Less population in the center clearly indicates a phase correlation. As the bunch-by-bunch feedback is switched on again at ≈ 33 ms, the coherent oscillation is starting to be damped. The process looks almost linear. Some bunches seem to be tamed right away as the center becomes more populated from ≈ 36 ms on. Yet extreme flanks start to arise at ≈ 42 ms. The vertically uniform filling reveals an incoherent oscillation which seems to become more populated as time passes. The decrease of the amplitude corresponds to a natural damping time $\tau_s \approx 36$ ms at 1.2 GeV beam energy. The incoherent oscillations remain long after the coherent oscillation was damped by the feedback system. This result is expected when comparing to section 2.1.1.

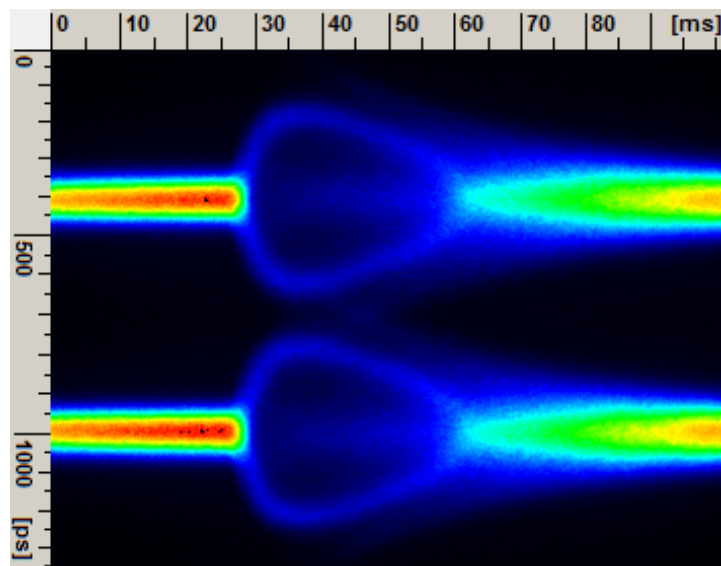


Figure 4.10: Grow-damp measurement at 1.2 GeV. The coherent oscillations are quickly damped by the feedback system. After ≈ 10 ms incoherent oscillations arise. They are naturally damped after $\tau_s \approx 36$ ms.

Another example is depicted in Fig. 4.11. At 1.9 GeV beam energy the coherent longitudinal oscillation was damped quickly and no incoherent oscillations arose. However, multiple coherent re-excitements can be observed. 35 ms after excitation, the exponential decay of the incoherent oscillations is again visible. The beam then returns to initial stability.

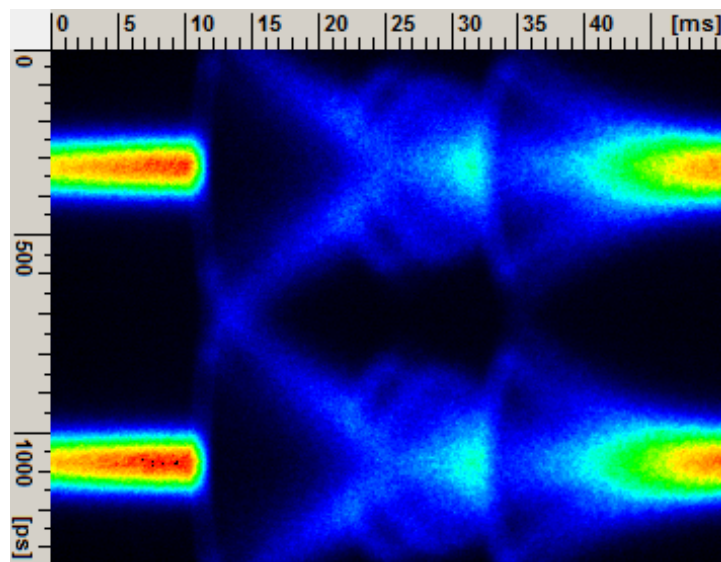


Figure 4.11: Fast coherent damping and multiple re-excitements at a 1.9 GeV grow-damp measurement.

4.2.3 ELSA at High Beam Currents

The ELSA pulse stretcher ring is currently optimized for circulating beam currents of around 30 mA. In storage mode a beam current of 115 mA was injected at 1.2 GeV. At the time, the bunch-by-bunch feedback system was not calibrated for high currents, hence Fig. 4.12 shows the natural longitudinal instability of the accelerator.

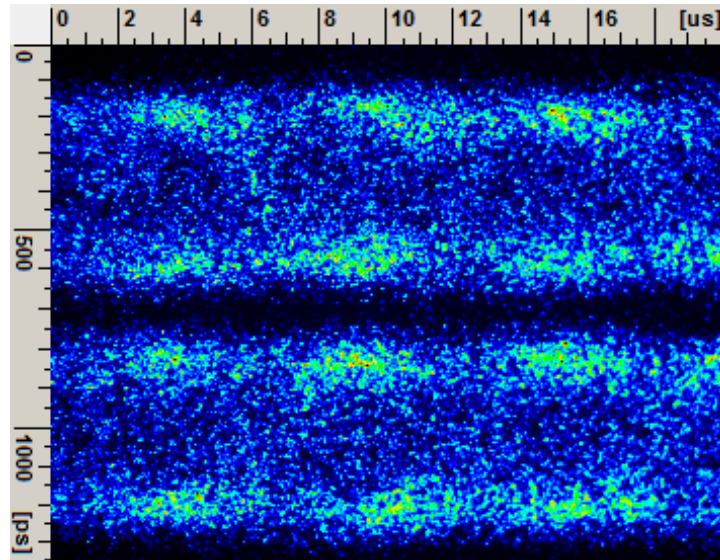


Figure 4.12: Longitudinal beam instability at 115 mA beam current in storage mode.

The structure weakly reveals two somewhat outstanding sine waves, approximately shifted in phase by π . The observable wavelength corresponds somewhat to $\lambda_s = 1/f_s \approx 11 \mu\text{m}$. Since the image consists of many overlapping signals, one may conclude that at least some parts of the bunch train coherently oscillate with the corresponding phase difference of π .

Summary and Outlook

The streak camera system has been installed at ELSA in late May 2013. Beamline development could however not be completed until mid October 2013. Restricted access to the experimental set-up area and an unfortunate vacuum leakage in the beamline delayed further commissioning. First long-term camera testing could be performed on October 25th 2013.¹ The streak camera system performed well, yet minor communication problems – likely due to the fiberglass extension – are to be solved in accordance to the manufacturer.

The streak camera system has proven its capability of resolving beam dynamics transversally and longitudinally on time scales from milliseconds down to nanoseconds. Precise bunch length measurements were performed at ELSA for the first time. It demonstrated good agreement with the predictions from the theory of particle accelerator physics. The streak camera is the only diagnosis tool available which is capable of detecting incoherent instabilities.

The M7 optical transfer beamline satisfies the streak camera's requirements for integrated measurements. Single shot measurements however suffer from poor signal to noise ratio.

The measured radiation levels at the back of the streak camera motivate the set-up of additional shielding. It should be noted that the optical table may not be suited for heavy loads. Further investigations are encouraged.

Extensive streak camera analysis of the *post-accelerator-mode* is encouraged in order to document the current beam stability on microscopic time scales.

The commissioning of an electron extraction beamline located close to the streak camera setup is currently taking place. A simulation of potential stray radiation should be performed in order to approximate future radiation levels. Additional shielding may be relevant.

Possible upgrades enhancing the beamline performance are:

- Installation of a variable set of magnifying lens pairs accounting for the difference of vertical and horizontal beam size. Remote controlled components are commercially available. However, the space available at the front of the streak camera is limited.
- A 50 % optical bypass around the Dove prism would enable simultaneous imaging of vertical and horizontal planes. Slow sweep measurements are usually thin streaks leaving a fair amount of horizontal imaging space unused. Coupling studies on fast time scales could be performed this way.

¹ The reader may compare this date to the submission date of this document

- In order to increase the light intensity the secondary deflecting mirror should be replaced by a larger reflecting surface. The increase of intensity is yet limited by other apertures in the vertical chicane. Detailed alignment studies are encouraged in order to provide feasible solutions concerning an intensity upgrade. One has to keep in mind the tedious work concerning readjusting the optics.
- Dispersion due to the use of affordable transmitting optics has not seemed to be an issue so far. However, reflective optics such as *off-axis parabolic mirrors* would be a more expensive alternative.
- The trigger signals for the streak camera are currently transmitted by two >100 m long RG-58 coaxial cables. Attenuation at high frequencies flattens the TTL trigger signals. A better slow sweep resolution may be achieved by replacing the corresponding cable.

The streak camera system is expected to detect manifold kinds of beam instabilities responsible for the limitation of beam current and quality.

Once single bunch injection becomes available, the streak camera will be of great use for the documentation of current dependent effects such as bunch lengthening or bunch asymmetry.

Appendix

A.1 Technical Drawing of the M7 dipole section

A.2 Streak Camera Photo Cathode Response

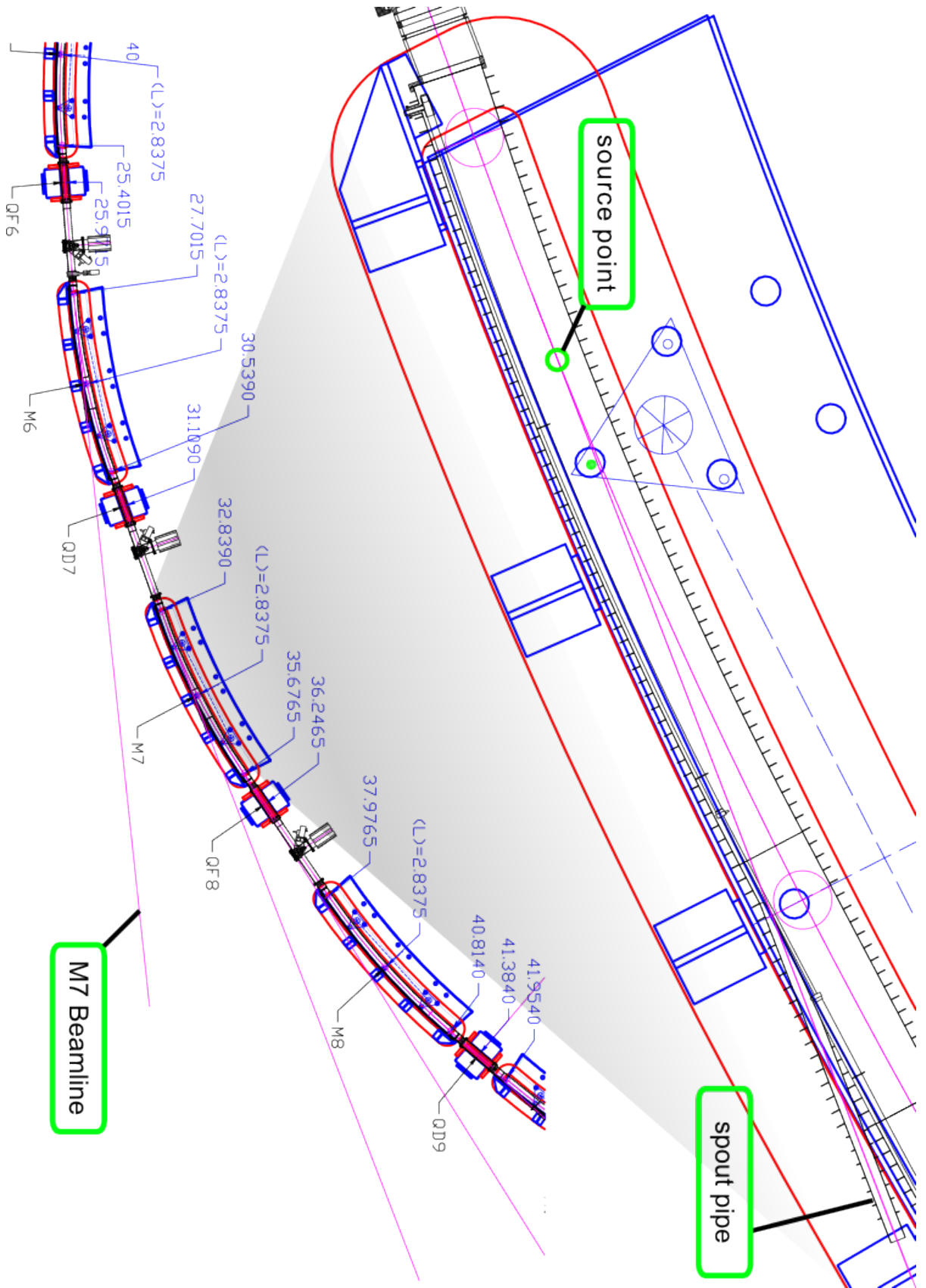


Figure A.1.: Drawing of the M7 dipole including the source point of the adjacent diagnosis beamline.

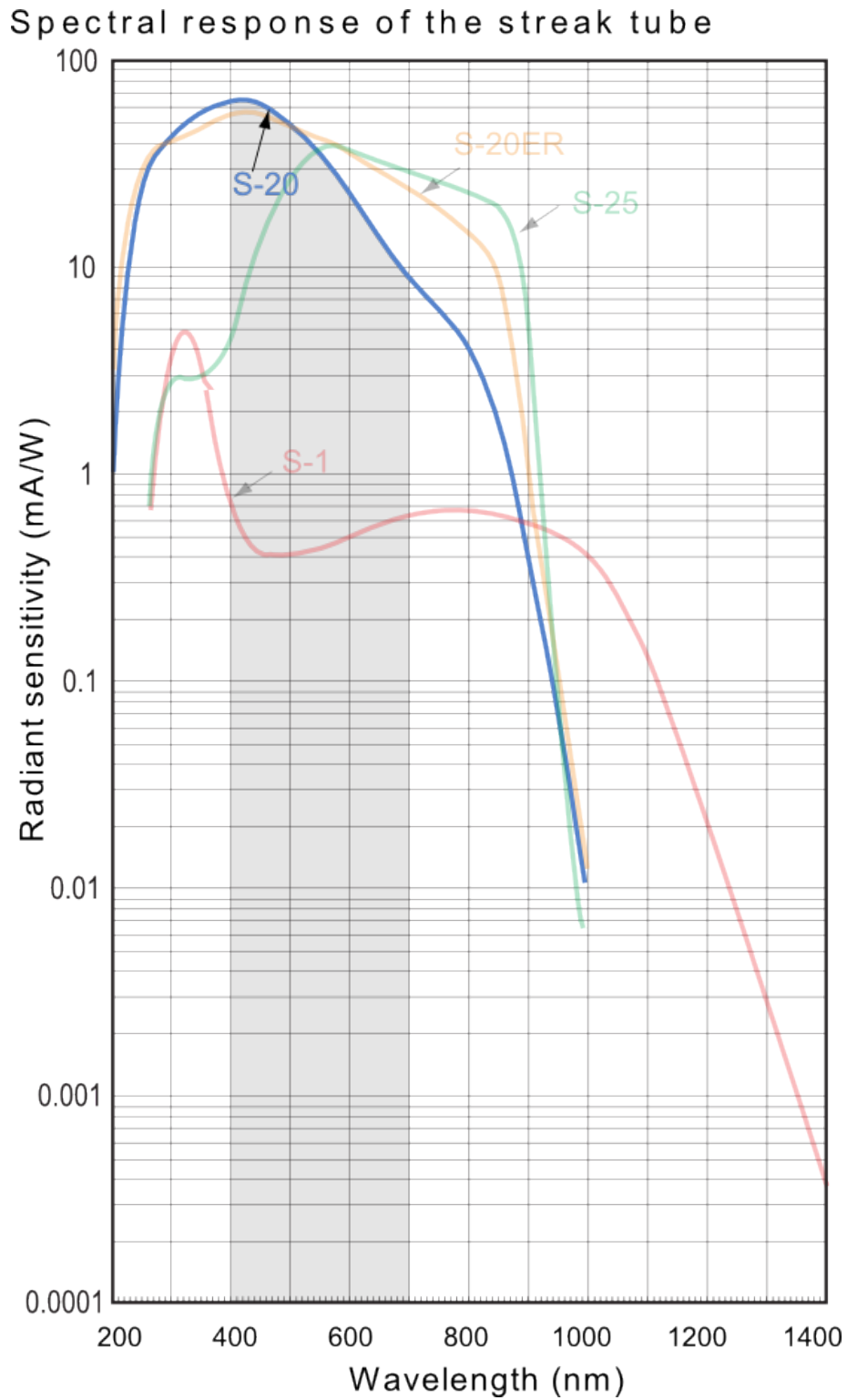


Figure A.2: Response function of the S-20 streak camera photo cathode.

Bibliography

- [HIL06] HILLERT, W., “The Bonn Electron Stretcher Accelerator ELSA: Past and Future”, *The European Physical Journal A - Hadrons and Nuclei* A.28 (2006) 139–148.
- [ALT67] ALTHOFF, K. H., “The 2.5 GeV Electron Synchrotron of the University of Bonn”, *Nuclear Instruments and Methods* 61 (1967) 1–30.
- [THOb] THOMA, U., *SFB/TRR 16 Subnuclear Structure of Matter*, <http://sfb-tr16.physik.uni-bonn.de/vfs/en/homepage/>.
- [THO05] THOMA, U., “Physics at ELSA, achievements and future”, *World Scientific, Proceedings of the 10th International Symposium on Meson-Nucleon Physics and the Structure of the Nucleon* (2005).
- [SCH10] SCHMIEDEN, H., “The BGO-OpenDipole setup at ELSA”, *International Journal of Modern Physics E*.19 (2010) 1043–1054.
- [THOa] THOMA, U., *D.2 Beam and spin dynamics in a fast ramping stretcher ring*, <http://sfb-tr16.physik.uni-bonn.de/vfs/en/projects/d2/>.
- [JAC98] JACKSON, J.D., *Classical Electrodynamics, Third Edition*, John Wiley & Sons, Inc., 1998.
- [WIL86] WILLE, K., *Physik der Teilchenbeschleuniger und Synchrotronstrahlungsquellen, 2. überarbeitete Ausgabe*, Teubner Studienbücher, 1986.
- [LEE04] LEE, S.Y., *Accelerator Physics, Second Edition*, World Scientific Publishing, 2004.
- [EBE10] EBERHARDT, M., “Messung und Korrektur der Arbeitspunkte während der Energierampe am Stretcherring von ELSA”,
PhD thesis: Rheinische-Friedrich-Wilhelms-Universität Bonn, 2010.
- [WIE95] WIEDEMANN, H.,
Particle Accelerator Physics - Basic Principles and Linear Beam Dynamics, 1. Auflage, Springer Verlag, 1995.
- [BER06] BERGSTROM, J., “The optical diagnostic beamline at the Canadian Light Source”, *Nuclear Instruments and Methods in Physics Research* (2006).
- [ZAN08] ZANDER, S.,
“Strahldiagnose mit Synchrotronlichtmonitoren an der Elektron-Stretcher-Anlage ELSA”,
MA thesis: Rheinische-Friedrich-Wilhelms-Universität Bonn, 2008.
- [ZAN13] ZANDER, S., “Optische Strahldiagnose an der Elektronen-Stretcher-Anlage ELSA”,
PhD thesis: Rheinische-Friedrich-Wilhelms-Universität Bonn, 2013.

- [FOR02] FOREST, E. und SCHMIDT, F. und MCINTOSH, E.,
“Introduction to the Polymorphic Tracking Code”,
European Organization for Nuclear Research CERN-SL-2002-044 (2002).
- [PRO11] PROFT, D.,
“Aufbau eines Monitorsystems zur Erfassung von Strahlverlust am ELSA-Stretcherring”,
MA thesis: Rheinische-Friedrich-Wilhelms-Universität Bonn, 2011.
- [HAE11] HAENISCH, P.,
“Konstruktion eines Spiegels für einen Synchrotronlichtmonitor mit FEM Unterstützung”,
MA thesis: Fachhochschule Köln, 2011.
- [SOL82] SOLLER, K.,
“Kohlenstoffkontamination der Oberflächen optischer Elemente im Synchrotronlicht”,
MA thesis: Universität Hamburg, 1982.
- [THOc] THORLABS Inc., *Data sheet Dove Prism PS993*.
- [HAM] HAMAMATSU Photonics K.K., *Universal streak camera C10910, test report*.
- [THOd] THORLABS Inc., *Data sheet Dove Prism PS993*.
- [Sch] *Data sheet SCHOTT N-BK7 glass*, URL: http://edit.schott.com/advanced_optics/english/abbe_datasheets/schott_datasheet_n-bk7.pdf.
- [ROT12] ROTH, A., “Breitbandige Feedback-Systeme zur Dämpfung kohärenter Strahlinstabilitäten am Stretcherring ELSA”,
PhD thesis: Rheinische-Friedrich-Wilhelms-Universität Bonn, 2012.

List of Figures

1.1	Facility drawing of the ELSA accelerator laboratory.	3
2.1	Coordinate system used for particle tracking in circular machines.	6
2.2	<i>Twiss</i> -parameters α , β and γ describing the orientation and size of the phase space ellipse.	7
2.3	Theoretical dispersion $D(s)$ and functions $\beta_x(s)$ and $\beta_z(s)$ throughout the full length of ELSA during the slow extraction process. The tunes are $Q_x = 4.63$ and $Q_z = 4.39$	8
2.4	Longitudinal incoherent oscillations of the electrons distribution around the synchrotron phase ψ_s at the accelerating voltage U_{acc} . momentum deviation causes particles to propagate on dispersive orbits.	10
2.5	Calculation of the angular power distribution as given by Eq. (2.39) at $\beta = 0.9$	14
2.6	An observer sees the emitted light of particles between point P_0 and P_1	14
2.7	Frequency spectrum of the radiated flux for different electron beam energies.	15
2.8	Schematic functionality principle of a streak camera.	18
2.9	Schematic drawing of the synchroscan principle with dual time base extension and typical measurement result. The red dots mark an incident light pulse swept across the phosphorous screen.	19
3.1	$\beta_{x,z}(s)$ and $D_x(s)$ around the source point s_0 of the M7 beamline. The source point is marked in red.	22
3.2	Photograph taken downwards onto the base plate (a) of the secondary deflecting mirror during illumination. The mirror aperture is smaller than the dimension of the light bundle, thus stray light (b) and the mirror's elliptical shadow (c) are clearly visible. The vertical aperture is defined by the slit system, as the blurry edges at top and bottom (d) indicate. Yet another aperture seems to cut off horizontal parts of the light. (e) may be an image of the round beam pipe of the vertical chicane. The flat edge (f) may be caused by the finite width of the primary deflecting mirror.	24
3.3	Overview of the M7 diagnostics beamline. An adjustable rectangular aperture is located ≈ 3 m downstream from the source point. The long beam pipe ensures a pressure gradient providing an ultra-high vacuum at the primary reflecting mirror at the end of the pipe. The synchrotron light exits the vacuum vertically through a fused silica glass window and enters an optically sealed box.	25
3.4	Optics layout close to scale. A dichroic mirror separates the UV from visible synchrotron light. The broad band visible light is magnified, rotated and attenuated before guided onto the streak camera's input optics.	26
3.5	Photograph of the M7 beamline diagnostic section. The light path is visualized for broad band (red) and narrow band UV light (purple).	29

3.6	Streak camera block diagram.	30
4.1	Slow sweep across $5 \mu\text{s}$: Top view of a slightly inhomogeneous filling pattern of 10 bunch trains.	31
4.2	Slow sweep across $1 \mu\text{s}$: The beam was distorted by the RF system, the repetitive filling gap is clearly visible.	32
4.3	Slow sweep across 100 ns: The fine structure of the beam is visible (side view).	32
4.4	Slow sweep across 200 ns: Single shot image of horizontal beam displacements.	33
4.5	Slow sweep across 20 ns: Single shot image of vertical beam displacements.	33
4.6	Synchroscan across 60ns: Resolution of single bunches. Note that the image was integrated over several turns in order to obtain a decent signal to noise ratio.	34
4.7	The bunch length σ_s increases linearly with energy when ω_s is kept constant. The solid line marks the calculated bunch length for $f_s = 88 \text{ kHz}$	34
4.8	Bunch length and phase dependency on beam energy with constant cavity voltage U_0	35
4.9	The dependency of bunch length and phase shift on beam energy matches the expected values.	36
4.10	Grow-damp measurement at 1.2 GeV. The coherent oscillations are quickly damped by the feedback system. After $\approx 10 \text{ ms}$ incoherent oscillations arise. They are naturally damped after $\tau_s \approx 36 \text{ ms}$	37
4.11	Fast coherent damping and multiple re-excitements at a 1.9 GeV grow-damp measurement.	37
4.12	Longitudinal beam instability at 115 mA beam current in storage mode.	38
A.1	Drawing of the M7 dipole including the source point of the adjacent diagnosis beamline.	42
A.2	Response function of the S-20 streak camera photo cathode.	43

List of Tables

2.1	ELSA pulse stretcher ring parameters	13
3.1	Source point beam parameters for the M7 diagnostic beamline.	22
3.2	Expected beam dimensions at the M7 source point for different beam energies E	22
3.3	Horizontal photon emission angles.	23
3.4	Magnitude of broadening at $\lambda = 400$ nm.	23
3.5	Available sweep units with corresponding time scales and purpose.	30

Acknowledgements

Foremost, I would like to express my sincere gratitude to all who have provided good advice for the success and final outcome of this project.

I owe my profound gratitude to my supervisor Priv.-Doz. Dr. W. Hillert for the useful comments, remarks and engagement through the learning process of this master thesis.

Furthermore I would like to thank Prof. Dr. J. Dingfelder for the support as a co-examiner.

Special thanks are given to Dr. F. Frommberger for his scientific advice and knowledge and many insightful discussions and suggestions.

I am also grateful to Dipl.-Ing-. P. Hänisch who has supplied me with technical and mechanical support with great patience.

Dr. A. Diekmann and Dipl.-Ing. F. G. Engelmann I would like to thank for providing support in electro-technical and facility specific matters.

I appreciate all staff members of the technical department of ELSA.

Also, I like to thank all my colleagues, who have willingly shared their precious time during the process of discussion, proofreading and finalizing this thesis. I have to acknowledge Sven Zander, Oliver Boldt, Dennis Proft, Dennis Sauerland, Jens-Peter Thiry, Jan Schmidt, Manuel Schedler, Christine Reinsch, Dominik Heiliger, Moritz Wiesner, Tobias Schiffer, Thorsten Pusch, Nicolas Heurich, Thomas Perlitius, Jens Zappai and Rebecca Koop. Thanks for giving me the opportunity to be part of the ELSA team- the group has been a source of friendships as well as good advice and collaboration.

I would like to thank my loved ones, who have supported me throughout the entire process, both by keeping me harmonious and helping me putting pieces together.

The most special thanks goes to my girlfriend. Sonja, you gave me your unconditional support and love through all this long process. Thanks for all your love and attention.